



The SILCC (SImulating the LifeCycle of molecular Clouds) project – I. Chemical evolution of the supernova-driven ISM

S. Walch,¹★ P. Girichidis,² T. Naab,² A. Gatto,² S. C. O. Glover,³
R. Wünsch,⁴ R. S. Klessen,^{3,5,6} P. C. Clark,⁷ T. Peters,^{2,8} D. Derigs¹
and C. Baczyński³

¹*I. Physikalisches Institut, Universität zu Köln, Zülpicher Str. 77, D-50937 Köln, Germany*

²*Max-Planck-Institute for Astrophysics, Karl-Schwarzschild-Str. 1, D-85741 Garching, Germany*

³*Zentrum für Astronomie der Universität Heidelberg, Institut für Theoretische Astrophysik, Albert-Ueberle-Str. 2, D-69120 Heidelberg, Germany*

⁴*Astronomical Institute, Academy of Sciences of the Czech Republic, Boční II 1401, CZ-141 31 Prague, Czech Republic*

⁵*Department of Astronomy and Astrophysics, University of California, 1156 High Street, Santa Cruz, CA 95064, USA*

⁶*Kavli Institute for Particle Astrophysics and Cosmology, Stanford University, SLAC National Accelerator Laboratory, Menlo Park, CA 94025, USA*

⁷*School of Physics & Astronomy, Cardiff University, 5 The Parade, Cardiff CF24 3AA, Wales, UK*

⁸*Institut für Computergestützte Wissenschaften, Universität Zürich, Winterthurerstrasse 190, CH-8057 Zürich, Switzerland*

Accepted 2015 August 24. Received 2015 August 24; in original form 2014 December 8

ABSTRACT

The SILCC (SImulating the Life-Cycle of molecular Clouds) project aims to self-consistently understand the small-scale structure of the interstellar medium (ISM) and its link to galaxy evolution. We simulate the evolution of the multiphase ISM in a $(500 \text{ pc})^2 \times \pm 5 \text{ kpc}$ region of a galactic disc, with a gas surface density of $\Sigma_{\text{GAS}} = 10 \text{ M}_\odot \text{ pc}^{-2}$. The FLASH 4 simulations include an external potential, self-gravity, magnetic fields, heating and radiative cooling, time-dependent chemistry of H₂ and CO considering (self-) shielding, and supernova (SN) feedback but omit shear due to galactic rotation. We explore SN explosions at different rates in high-density regions (*peak*), in random locations with a Gaussian distribution in the vertical direction (*random*), in a combination of both (*mixed*), or clustered in space and time (*clus/clus2*). Only models with self-gravity and a significant fraction of SNe that explode in low-density gas are in agreement with observations. Without self-gravity and in models with *peak* driving the formation of H₂ is strongly suppressed. For decreasing SN rates, the H₂ mass fraction increases significantly from <10 per cent for high SN rates, i.e. 0.5 dex above Kennicutt-Schmidt, to 70–85 per cent for low SN rates, i.e. 0.5 dex below KS. For an intermediate SN rate, *clustered* driving results in slightly more H₂ than random driving due to the more coherent compression of the gas in larger bubbles. Magnetic fields have little impact on the final disc structure but affect the dense gas ($n \gtrsim 10 \text{ cm}^{-3}$) and delay H₂ formation. Most of the volume is filled with hot gas (~ 80 per cent within $\pm 150 \text{ pc}$). For all but *peak* driving a vertically expanding warm component of atomic hydrogen indicates a fountain flow. We highlight that individual chemical species populate different ISM phases and cannot be accurately modelled with temperature-/density-based phase cut-offs.

Key words: MHD – ISM: clouds – ISM: evolution – ISM: structure – ISM: supernova remnants – galaxies: ISM.

1 INTRODUCTION

Within a typical disc galaxy, gas is continually cycled between several very different phases. Warm atomic gas cools and undergoes gravitational collapse, forming cold, dense molecular clouds. Stars

form in many of these clouds and exert strong feedback on the surrounding gas, in the form of UV radiation (Dale et al. 2005; Dale, Ercolano & Bonnell 2012; Walch et al. 2012, 2013), stellar winds (Toalá & Arthur 2011; Rogers & Pittard 2013), and supernova (SN) explosions (Hill et al. 2012; Gatto et al. 2015; Kim & Ostriker 2015; Martizzi, Faucher-Giguère & Quataert 2015; Walch & Naab 2015). This feedback helps to disperse many of the clouds, returning gas to the warm atomic phase, or heating it so much that it reaches a

* E-mail: walch@ph1.uni-koeln.de

highly diffuse, ionized phase. Other clouds are destroyed by large-scale dynamical processes in the disc, such as the strong shear flows around spiral arms (see e.g. Dobbs & Pringle 2013). Dynamically significant magnetic fields help to guide the gas flows that form and disperse the clouds (e.g. de Avillez & Breitschwerdt 2004, 2005; Banerjee et al. 2009; Heitsch, Stone & Hartmann 2009), and cosmic rays can also play an important role, as they represent a significant fraction of the local energy density in the interstellar medium (ISM; e.g. Breitschwerdt 2008; Dorfi & Breitschwerdt 2012; Hanasz et al. 2013; Girichidis et al. 2014b).

Understanding how gas is cycled between the different phases in the ISM and how molecular clouds are formed and destroyed is important for understanding how star formation is regulated in galaxies. The interplay between feedback from massive stars and the surrounding ISM also governs the launching of galactic winds, which play an important role for regulating spiral galaxy evolution on larger spatial and temporal scales at all cosmic epochs (Oppenheimer et al. 2010; Aumer et al. 2013; Hirschmann et al. 2013; Stinson et al. 2013; Brook et al. 2014; Hopkins et al. 2014; Marinacci, Pakmor & Springel 2014; Übler et al. 2014; Murante et al. 2015). Substantial effort has already been devoted to the study of stellar feedback and the regulation of star formation on galactic scales (see e.g. Stinson et al. 2010; Hopkins, Quataert & Murray 2011, Agertz et al. 2013, and Genel et al. 2014 for a few recent examples), but much of this work considers only large scales and fails to resolve the small-scale processes responsible for driving the large-scale flows.

A better understanding of the ISM is therefore of fundamental astrophysical importance. However, the ISM is governed by a complex network of many interacting physical processes. Any of these processes alone can affect the properties of the ISM significantly and their mutual interaction may well be non-linear. For a comprehensive model of the ISM, it is therefore important to consider all of the above processes (heating, cooling, gravity, chemistry, magnetic fields, etc.), but for a concise understanding it is necessary to first investigate their impact separately. Within the framework of SILCC (SImulating the Life-Cycle of molecular Clouds¹), we have started this enterprise as a collaboration in which we aim to understand the full life-cycle of molecular clouds using state-of-the-art numerical simulations. In this first SILCC paper, we introduce the elements of our numerical model, and use it to study the effect of the spatial and temporal distribution of SN explosions on the multiphase structure of the ISM and the formation of molecular gas.

Specifically, we use the adaptive mesh refinement (AMR) code FLASH 4 to model the multiphase ISM in a representative portion of a disc galaxy in three-dimensional, magnetohydrodynamic (MHD) simulations, including

- (i) an external galactic potential,
- (ii) self-gravity,
- (iii) radiative heating and cooling coupled to
- (iv) a chemical network to follow the formation of H₂ and CO,
- (v) diffuse heating and its attenuation by dust shielding, and
- (vi) feedback from SN explosions of massive stars.

This setup allows us to self-consistently follow the formation and evolution of molecular clouds in disc galaxies. Since much of the gas in the ISM is highly turbulent and out of chemical equilibrium, it is necessary to follow molecule formation on-the-fly, even though

this process has only a minor impact on the gas dynamics (Glover & Clark 2012a).

In this paper, we investigate the specific location and clustering properties of the SNe on the structure of the multiphase ISM and in particular on the evolution of the molecular gas phase. We study four different models for SN driving: (1) SNe explode at random positions, modulo the constraint that the positions form a Gaussian distribution in the vertical direction about the disc mid-plane with a scaleheight of 50 pc; (2) SNe explode within forming molecular clouds, i.e. at the peaks in the density distribution; (3) half of the SNe explode randomly, and half of them explode within dense clouds (mixed driving); or (4) the SNe explode in clusters and are therefore correlated in space and time (e.g. Mac Low & McCray 1988; Matzner 2002). We also modify point (4) and investigate the effect of a clustered distribution of Type II SNe and a more extended component of Type Ia's with a scaleheight of 325 pc. These different driving mechanisms have been employed in previous studies (see below), but a conclusive comparison between them has not yet been carried out.

Previously, many groups have investigated the development of the multiphase ISM structure in a representative portion (with similar size to our setup) of a stratified galactic disc. In particular, Joung & Mac Low (2006), Hill et al. (2012), Gent et al. (2013a), Gent et al. (2013b), and Creasey, Theuns & Bower (2013) have carried out simulations of stratified discs with the FLASH code (although older releases of it), employing mostly randomly placed or clustered SNe. They ran models with and without self-gravity (although these are not compared in the way presented here) as well as with and without magnetic fields and found that the magnetic field is generally unimportant for the global disc structure. Recently, Hennebelle & Iffrig (2014) computed models of low surface density discs with $\Sigma_{\text{GAS}} \sim 3 M_{\odot} \text{ pc}^{-2}$ and galactic SN rates with RAMSES (Teyssier 2002). They include magnetic fields and self-gravity, which leads to the formation of sink particles, and show that a weak magnetic field (2.5 μG) reduces the star formation rate (SFR) by a factor of ~ 2 .

The setup used in the work of Kim, Kim & Ostriker (2011), Shetty & Ostriker (2012), and Kim, Ostriker & Kim (2013), carried out with the ATHENA MHD code (Stone et al. 2008), is different since they correlate SN explosions with dynamically forming, local density maxima, and include shearing box boundary conditions. The SNe deposit a fixed amount of momentum ($3 \times 10^5 M_{\odot} \text{ km s}^{-1}$ per event) into the surrounding gas, but no thermal energy is added, and thus there is no hot gas present in these simulations. With this method, the SFR within the discs can be regulated to the observed level. The role of shear – which we do not include at the moment – is potentially important, in particular for gas-rich disc models (Shetty & Ostriker 2012), which resemble the conditions within the Galactic Center or in high-redshift, star-forming galaxies (Förster Schreiber et al. 2011; Genzel et al. 2011; Fisher et al. 2013). In these environments, shear could limit the size of the cold clouds that form. Models of full galactic discs (Dobbs, Pringle & Burkert 2012; Bonnell, Dobbs & Smith 2013) even describe shear as one of the main drivers of ISM turbulence (e.g. Piontek & Ostriker 2005; Kevlahan & Pudritz 2009; and see Agertz et al. 2009 for a discussion), although the main role of the spiral arm structure to form and cause collisions between molecular clouds is also emphasized. A detailed investigation of the relative contribution of shear will be left to future study.

Most of the models discussed above use highly simplified cooling functions and do not follow the formation of molecular gas. A few attempts have been made to account for the non-equilibrium

¹ For movies of the simulations and download of selected FLASH data see the SILCC website: <http://www.astro.uni-koeln.de/silcc>

chemistry of H₂ within galactic-scale simulations of the ISM (see e.g. Dobbs et al. 2008; Gnedin, Tassis & Kravtsov 2009; Dobbs, Burkert & Pringle 2011; Christensen et al. 2012), and more recently a couple of studies have also treated CO formation (Pettitt et al. 2014; Smith et al. 2014). However, the spatial and mass resolution in most of these studies is poor (with the exception of the recent simulations by Smith et al. (2014), which have a mass resolution of only 4 M_⊙, but these simulations did not account for either stellar feedback or for the self-gravity of the gas).

In this paper, we improve on this earlier work by combining high-resolution AMR simulations that properly account for the effects of magnetic fields, SN feedback and self-gravity with a non-equilibrium treatment of the H₂ and CO chemistry of the gas. The plan of this paper is the following. The numerical method is described in Section 2, and the simulation setup, the SN positioning, and the adopted SN rates are outlined in Section 3. In Section 4, we discuss the morphologies and chemical evolution of simulations that use the same SN rate but different physics or SN positioning. The influence of the SN rate is discussed in Section 5, and Section 6 shows the vertical distributions and the evolution of the disc in the *z*-direction. In Section 7, we show the difference between temperature phases and the chemical composition of the gas. We summarize our findings with respect to the total gas mass fractions in the different chemical species and the average volume filling fractions of the different temperature phases in Section 8, and give our conclusions in section 9.

2 NUMERICAL METHOD

We use the fully three-dimensional, AMR code FLASH 4 (Fryxell et al. 2000; Dubey et al. 2009, 2012) to simulate representative pieces of galactic discs with dimensions 500 pc × 500 pc × ±5 kpc. FLASH is parallelized via domain decomposition under the Message Passing Interface (MPI). It further employs a finite volume scheme, in which the physical variables are represented as zone averages. The AMR is handled by the PARAMESH library.

2.1 Magnetohydrodynamics

Using FLASH 4, we model the evolution of the gas via solving the ideal MHD equations. For all simulations (magnetic and non-magnetic), we use a directionally split, finite-difference scheme that is based on the 5-wave Bouchut MHD solver HLL5R (Bouchut, Klingenberg & Waagan 2007; Klingenberg, Schmidt & Waagan 2007; Waagan 2009; Bouchut, Klingenberg & Waagan 2010; Waagan, Federrath & Klingenberg 2011), which is stable and preserves positivity for high Mach number flows. The non-linear flux of quantities between zones is obtained by solving a Riemann problem at each zone boundary in alternating one-dimensional sweeps through the grid (MUSCL scheme; VanLeer 1979). With (self-)gravity (see Section 2.4), the equations read

$$\frac{\partial \rho}{\partial t} + \nabla \cdot (\rho \mathbf{v}) = 0, \quad (1)$$

$$\frac{\partial \rho \mathbf{v}}{\partial t} + \nabla \cdot \left[\rho \mathbf{v} \mathbf{v}^T + \left(P + \frac{\|\mathbf{B}\|^2}{8\pi} \right) \mathbf{I} - \frac{\mathbf{B} \mathbf{B}^T}{4\pi} \right] = \rho \mathbf{g} + \dot{q}_{\text{inj}}, \quad (2)$$

$$\frac{\partial \mathbf{B}}{\partial t} - \nabla \times (\mathbf{v} \times \mathbf{B}) = 0. \quad (3)$$

Here, *t* is the time, ρ is the mass density, \mathbf{v} is the gas velocity, \mathbf{B} is the magnetic field, and $P = (\gamma - 1)u$ is the thermal pressure, where u is the internal energy per unit volume. We assume an ideal

gas with $\gamma = 5/3$. \mathbf{I} is the 3×3 identity matrix, and $\mathbf{B} \mathbf{B}^T$ is the outer product of \mathbf{B} with itself. The divergence-free constraint applies ($\nabla \cdot \mathbf{B} = 0$). The momentum input from SNe per time step is \dot{q}_{inj} . The gravitational acceleration \mathbf{g} combines the contributions from the self-gravity of the gas (\mathbf{g}_{sg} ; see Section 2.4), and from the external gravitational potential (\mathbf{g}_{ext} ; see Section 3.2), which is provided by the stellar distribution within the galactic disc:

$$\mathbf{g} = \mathbf{g}_{\text{sg}} + g_{\text{ext}}(z)\hat{z}. \quad (4)$$

We modify the energy equation to include heating and cooling effects as well as the energy input by SNe:

$$\begin{aligned} \frac{\partial E}{\partial t} + \nabla \cdot \left[\left(E + \frac{\|\mathbf{B}\|^2}{8\pi} + \frac{P}{\rho} \right) \mathbf{v} - \frac{(\mathbf{B} \cdot \mathbf{v}) \mathbf{B}}{4\pi} \right] \\ = \mathbf{v} \cdot \mathbf{g} + \dot{u}_{\text{chem}} + \dot{u}_{\text{inj}}, \end{aligned} \quad (5)$$

where the energy density (in erg per unit volume) is

$$E = u + \frac{\rho \|\mathbf{v}\|^2}{2} + \frac{\|\mathbf{B}\|^2}{8\pi}. \quad (6)$$

\dot{u}_{chem} is the net rate of change in internal energy due to diffuse heating and radiative cooling, both of which are computed through the chemical network (as described in Section 2.2). \dot{u}_{inj} is the thermal energy input (per unit volume) from SNe. The detailed implementation of SN feedback is described in Section 3.3.1.

In the case of fast advection, where the kinetic energy dominates the internal energy by more than four orders of magnitude (parameter *eint_switch* = 10⁻⁴), we separately solve for the internal energy, *u*, to avoid truncation errors:

$$\frac{\partial u}{\partial t} + \nabla \cdot \left[\left(u + \frac{P}{\rho} \right) \mathbf{v} \right] = \mathbf{v} \cdot \nabla \left(\frac{P}{\rho} \right). \quad (7)$$

Then the total energy is recomputed using the velocities from the momentum equation as well as the new internal energy.

2.2 Chemistry and cooling

We follow the chemical evolution of the gas in our simulations using a simplified chemical network that tracks the ionization fraction of the gas, and the formation and destruction of H₂ and CO. We do not assume chemical equilibrium and therefore have to solve a continuity equation of the form (see e.g. Glover & Mac Low 2007a; Micic et al. 2012)

$$\frac{\partial \rho_i}{\partial t} + \nabla \cdot (\rho_i \mathbf{v}) = C_i(\rho, T, \dots) - D_i(\rho, T, \dots) \quad (8)$$

for every chemical species *i* included in our network. The terms C_i and D_i in this equation represent the creation and destruction of species *i* due to chemical reactions. These terms generally depend on the density and temperature of the gas, and also on the abundances of the other chemical species. Therefore, we have to solve a set of coupled partial differential equations for the mass densities of the different chemical species. In practice, we can make the problem substantially easier to handle by operator splitting the chemical source and sink terms from the advection terms. With this approach, the continuity equations that we have to solve during the advection step simplify to

$$\frac{\partial \rho_i}{\partial t} + \nabla \cdot (\rho_i \mathbf{v}) = 0. \quad (9)$$

These equations describe the evolution of a set of scalar tracer fields, and can be handled using the standard FLASH infrastructure for such fields. Changes in the chemical composition of the gas resulting

from chemical reactions are then computed in a separate chemistry step, during which we solve the following set of coupled ordinary differential equations (ODEs),

$$\frac{d\rho_i}{dt} = C_i(\rho, T, \dots) - D_i(\rho, T, \dots). \quad (10)$$

Because the radiative cooling rate can often depend sensitively on the chemical abundances, we also operator split the FLASH energy equation, solving for the rate of change in E due to radiative heating and cooling, \dot{u}_{chem} , separately from the other terms in equation (5). The resulting ODE describing \dot{u}_{chem} is solved simultaneously with the chemical ODEs, using the implicit solver DVODE (Brown, Byrne & Hindmarsh 1989). A similar basic approach was used in the ZEUS-MP MHD code by Glover et al. (2010) and in an earlier version of the FLASH code by Walch et al. (2011) and Micic et al. (2012, 2013).

If the chemistry or cooling time-steps are much shorter than the hydrodynamical time-step, then subcycling is used to treat the cooling and chemistry, thereby avoiding the need to constrain the global time-step. We limit the maximum size of the time-step taken within the ODE solver to be

$$\Delta t_{\text{max}} = \min(\Delta t_{\text{cool}}, \Delta t_{\text{chem}}), \quad (11)$$

where Δt_{cool} and Δt_{chem} are the cooling time-step and the chemical time-step, respectively, which are estimated using the current values of \dot{u}_{chem} , C_i and D_i .

The chemical network used in our simulations is based on the network for hydrogen chemistry presented in Glover & Mac Low (2007a,b), supplemented with the simplified model for CO formation introduced by Nelson & Langer (1997). We model the evolution of seven chemical species: free electrons, H^+ , H, H_2 , C^+ , O and CO. The fractional abundances of these species are constrained by several different conservation laws. We conserve total charge, allowing us to write the free electron abundance as

$$x_e = x_{\text{H}^+} + x_{\text{C}^+} + x_{\text{Si}^+}, \quad (12)$$

where x_i denotes the fractional abundance of species i , relative to the total abundance of hydrogen nuclei in all forms. Note that although we include a contribution from ionized silicon in our expression for x_e , we do not track the chemical evolution of silicon, instead simply assuming that it remains singly ionized throughout the gas. In addition to conserving charge, we also conserve the total abundances of hydrogen, carbon and oxygen, allowing us to derive the fractional abundances of atomic hydrogen, ionized carbon and atomic oxygen from the following expressions:

$$x_{\text{H}} = 1 - 2x_{\text{H}_2} - x_{\text{H}^+}, \quad (13)$$

$$x_{\text{C}^+} = x_{\text{C,tot}} - x_{\text{CO}}, \quad (14)$$

$$x_{\text{O}} = x_{\text{O,tot}} - x_{\text{CO}}, \quad (15)$$

where $x_{\text{C,tot}}$ and $x_{\text{O,tot}}$ are the total fractional abundances of carbon and oxygen (in all forms) relative to hydrogen. Using these relationships allows us to reduce the number of chemical species for which we need to solve the full chemical rate equations from seven to three: H^+ , H_2 and CO.

In our current set of simulations, we assume a constant gas-phase metallicity $Z = Z_{\odot}$ and a constant dust-to-gas ratio of 0.01. We take the total gas-phase carbon, oxygen and silicon abundances to be $x_{\text{C,tot}} = 1.41 \times 10^{-4}$, $x_{\text{O,tot}} = 3.16 \times 10^{-4}$ and $x_{\text{Si,tot}} = 1.5 \times 10^{-5}$ (Sembach et al. 2000).

2.2.1 Hydrogen chemistry

The full set of chemical reactions that make up our implementation of the non-equilibrium hydrogen chemistry are given in table 1 of Micic et al. (2012). We include the standard processes governing the formation and destruction of ionized hydrogen (collisional ionization, ionization by cosmic rays and X-rays, radiative recombination, etc.) plus a simplified treatment of H_2 formation and destruction. H_2 is assumed to form only on the surface of dust grains, following the prescription given in Hollenbach & McKee (1989), as this dominates over gas-phase formation via the H^- or H_2^+ ions at metallicities close to solar (Glover 2003). Some H_2 is destroyed by cosmic ray ionization and by collisional dissociation in hot gas, but in most regions, the dominant destruction process is photodissociation by the interstellar radiation field (ISRF). In our treatment, we compute the H_2 photodissociation rate using the following expression:

$$R_{\text{pd,H}_2} = R_{\text{pd,H}_2, \text{thin}} f_{\text{dust,H}_2} f_{\text{shield,H}_2}. \quad (16)$$

Here, $R_{\text{pd,H}_2, \text{thin}} = 3.3 \times 10^{-11} G_0 \text{ s}^{-1}$ is the photodissociation rate in optically thin gas, taken from Draine & Bertoldi (1996), G_0 is the strength of the ISRF in units of the Habing (1968) field, $f_{\text{dust,H}_2}$ is a factor accounting for the effects of dust extinction and $f_{\text{shield,H}_2}$ is a factor accounting for H_2 self-shielding. Along any particular line of sight, $f_{\text{dust,H}_2}$ is related to the visual extinction A_V by

$$f_{\text{dust,H}_2} = \exp(-3.5A_V). \quad (17)$$

In the diffuse ISM, A_V is related to the total hydrogen column density $N_{\text{H,tot}}$ by (Bohlin, Savage & Drake 1978)

$$A_V = \frac{N_{\text{H,tot}}}{1.87 \times 10^{21} \text{ cm}^{-2}}, \quad (18)$$

where $N_{\text{H,tot}} = N_{\text{H}^+} + N_{\text{H}} + 2N_{\text{H}_2}$. In dense clouds, grain coagulation leads to a slightly different relationship between A_V and $N_{\text{H,tot}}$ (see e.g. Foster et al. 2013), but we neglect this complication here.

To determine $f_{\text{shield,H}_2}$ for a particular line of sight, we use the following self-shielding function from Draine & Bertoldi (1996):

$$f_{\text{shield,H}_2} = \frac{0.965}{(1 + x/b_5)^2} + \frac{0.035}{\sqrt{1+x}} \times \exp\left(-8.5 \times 10^{-4}\sqrt{1+x}\right), \quad (19)$$

where $x = N_{\text{H}_2} / (5 \times 10^{14} \text{ cm}^{-2})$, $b_5 = b/(10^5 \text{ cm s}^{-1})$, and b is the Doppler broadening parameter, which is related to the gas temperature by $b^2 = k_{\text{B}}T/m_{\text{H}}$. We compute the values of $f_{\text{dust,H}_2}$ and $f_{\text{shield,H}_2}$ for each grid cell² by averaging over multiple lines of sight using the TREECOL algorithm (Clark, Glover & Klessen 2012), which we describe in more detail in Section 2.3.

2.2.2 Carbon chemistry

To model the transition from C^+ to CO, we use a highly simplified treatment first introduced by Nelson & Langer (1997, hereafter, NL97). Their approach is based on the assumption that the rate limiting step in the formation of CO is the radiative association of C^+ with H_2 to form the CH_2^+ molecular ion. Once formed, this ion is assumed to have only two possible fates: either it reacts with atomic oxygen to produce CO, or it is photodissociated by the ISRF, returning the carbon to the gas as C^+ . This model tends to overproduce

² We use the local temperature to estimate b , assuming that this is reasonably representative of the bulk temperature of H_2 along the line of sight. Note also, that $f_{\text{shield,H}_2}$ is only weakly dependent on b .

CO somewhat at intermediate densities and extinctions compared to more detailed chemical models (see e.g. the detailed comparison in Glover & Clark 2012b). However, we do not expect this to significantly affect the spatial distribution of CO or the temperature structure of the gas on the scales resolved in the set of simulations presented in this paper.

The main process responsible for destroying CO is photodissociation by the ISRF. We adopt a photodissociation rate given by

$$R_{\text{pd,CO}} = R_{\text{pd,CO,thin}} f_{\text{dust,CO}} f_{\text{shield,CO}} \text{ s}^{-1}. \quad (20)$$

Here, $R_{\text{pd,CO,thin}} = 2.1 \times 10^{-10} (G_0/1.7) \text{ s}^{-1}$ is the photodissociation rate of CO in optically thin gas, taken from van Dishoeck & Black (1988), $f_{\text{shield,CO}}$ is a shielding factor quantifying the effects of CO self-shielding and the shielding of CO by the Lyman–Werner bands of H₂, and f_{dust} accounts for the effects of dust absorption. To compute $f_{\text{shield,CO}}$ for a particular line of sight, we first compute the H₂ and CO column densities along that line of sight, and then convert these into a value for $f_{\text{shield,CO}}$ using data from Lee et al. (1996). For the dust absorption term $f_{\text{dust,CO}}$, we use the expression (van Dishoeck & Black 1988)

$$f_{\text{dust,CO}} = \exp(-2.5A_V) \quad (21)$$

using the same relationship as before between the visual extinction A_V and the total hydrogen column density $N_{\text{H,tot}}$. To compute $f_{\text{dust,CO}}$ and $f_{\text{shield,CO}}$ for each grid cell, we once again average their values over multiple lines of sight using the TREENCOL algorithm (see Section 2.3).

2.2.3 Radiative cooling

To model the effects of radiative cooling, we use the detailed atomic and molecular cooling function outlined in Glover et al. (2010) and updated in Glover & Clark (2012b). This includes contributions from the fine structure lines of C⁺, O and Si⁺, the rotational and vibrational lines of H₂ and CO, the electronic lines of atomic hydrogen (i.e. Lyman α cooling), and also the transfer of energy from the gas to the dust, although the latter effect is generally unimportant at the densities reached in these simulations. Since we do not explicitly track the ionization state of helium, or any ionization states of the metals beyond the singly ionized state of carbon, we cannot compute the contribution of these to the high-temperature cooling rate in a completely self-consistent fashion. Instead, we assume that at $T > 10^4$ K, the helium and the metals are in collisional ionization equilibrium, and determine their contribution to the cooling rate using the ion-by-ion cooling rates given in Gnat & Ferland (2012). Note that at no point do we assume that hydrogen is in collisional ionization equilibrium: its contribution to the cooling rate is determined self-consistently at all temperatures, allowing us to properly model the non-equilibrium effects that can strongly affect the cooling rate at temperatures close to 10⁴ K (see e.g. Kafatos 1973; Sutherland & Dopita 1993; Micic et al. 2013; Richings, Schaye & Oppenheimer 2014).

2.2.4 Radiative heating

We account for the radiative heating of the gas by cosmic rays, soft X-rays, and photoelectric emission from small grains and polycyclic aromatic hydrocarbons (PAHs). We adopt a cosmic ray ionization rate for neutral atomic hydrogen given by $\zeta_H = 3 \times 10^{-17} \text{ s}^{-1}$ and a rate twice this size for the cosmic ray ionization of H₂. The heating rate per unit volume due to cosmic ray ionization is then given by

$\Gamma_{\text{cr}} = 20 \zeta_H n \text{ eV s}^{-1} \text{ cm}^{-3} = 3.2 \times 10^{-11} \zeta_H n \text{ erg s}^{-1} \text{ cm}^{-3}$ (Goldsmith & Langer 1978). To account for X-ray heating and ionization, we use the prescription given in appendix A of Wolfire et al. (1995), assuming a fixed absorbing column of hydrogen $N_{\text{H}} = 10^{20} \text{ cm}^{-2}$. Finally, we model the effects of photoelectric heating using a heating rate given by (Bakes & Tielens 1994; Bergin et al. 2004)

$$\Gamma_{\text{pe}} = 1.3 \times 10^{-24} \epsilon G_{\text{eff}} n \text{ erg s}^{-1} \text{ cm}^{-3}, \quad (22)$$

where $G_{\text{eff}} = G_0 \exp(-2.5A_V)$, and where the photoelectric heating efficiency ϵ is given by (Bakes & Tielens 1994; Wolfire et al. 2003)

$$\epsilon = \frac{0.049}{1 + (\psi/963)^{0.73}} + \frac{0.037(T/10\,000)^{0.7}}{1 + (\psi/2500)}, \quad (23)$$

with

$$\psi = \frac{G_{\text{eff}} T^{1/2}}{n_e}. \quad (24)$$

To compute A_V , we use the same approach as described above in our discussion of the carbon chemistry.

2.2.5 Chemical heating and cooling

We account for changes in the thermal energy of the gas due to several different chemical processes: cooling from H⁺ recombination, the collisional ionization of H and the collisional dissociation of H₂, and heating from H₂ formation, H₂ photodissociation, and UV pumping of vibrationally excited states of H₂ by the ISRF. Full details of our treatment of these processes can be found in Glover & Mac Low (2007a,b) and Glover & Clark (2012b).

2.2.6 Dust

We self-consistently determine the dust temperature in every grid cell by assuming that the dust is in thermal equilibrium and solving for the dust temperature T_d for which the heating of the dust grains by the ISRF and by collisions with the gas is balanced by their thermal emission. We assume that the dust-to-gas ratio is 0.01, and that the dust has a size distribution typical for the Milky Way. For the dust opacities, we use values from Mathis, Mezger & Panagia (1983) for wavelengths shorter than 1 μm and from Ossenkopf & Henning (1994) for longer wavelengths. To treat the attenuation of the ISRF by dust absorption, which reduces the heating rate of the dust in dense regions of the ISM, we use the column density dependent attenuation factor $\chi(N_{\text{H}})$ computed by Glover & Clark (2012b), together with the values of N_{H} provided by the TREENCOL algorithm (see below).

2.3 Modelling molecular self-shielding and dust shielding using TREENCOL

In order to model the attenuation of the ISRF by H₂ self-shielding, CO self-shielding, the shielding of CO by H₂, and absorption by dust, we need a fast but accurate method for computing the column densities of hydrogen nuclei, H₂ and CO along many different sight-lines in our simulations. We do this by means of the TREENCOL algorithm (Clark et al. 2012). This algorithm uses information stored in the oct-tree structure that FLASH also uses to compute the effects of self-gravity (see Section 2.4) to compute 4π steradian maps of the dust extinction, and H₂ and CO column density distributions surrounding each grid cell in the computational domain. These maps are discretized on to N_{pix} equal-area pixels using the HEALPix algorithm (Górski & Hivon 2011). We can then compute values

of $f_{\text{dust}, \text{H}_2}$, $f_{\text{dust}, \text{CO}}$, χ , etc. for each pixel, as outlined above, and finally can determine a single mean value for each cell simply by taking the arithmetic mean of the values for the individual pixels. In the simulations presented here, we use $N_{\text{pix}} = 48$ pixels. We have explored the effects of increasing N_{pix} , but find that at our current level of hydrodynamical resolution, and with the employed tree opening angle, it makes little difference to the outcome of the simulations.

The version of TREECOL described in Clark et al. (2012) includes all of the gas between the grid cell of interest and the edge of the simulation volume in its calculation of the column densities. However, we cannot use the same approach in our present simulations, as we expect that the typical separation between individual UV sources at the given disc surface density will be much less than 500 pc. We therefore use a similar strategy to that used by Smith et al. (2014); we define a shielding length $L_{\text{sh}} = 50$ pc and only include gas located at $L \leq L_{\text{sh}}$ in our calculation of the column densities, where we allow the search radius to extend across periodic boundaries. In practice, we do not expect our results to be particularly sensitive to moderate variations in L_{sh} .

In addition, we have improved and optimized the algorithm of Clark et al. (2012) significantly, leading to a speedup of more than a factor of 10 with respect to the original implementation. Details of the FLASH implementation of TREECOL are presented in Wünsch et al., in preparation.

In the runs that we perform with our standard SN rate of 15 Myr⁻¹, we use the estimate of Draine (1978) for the strength of the UV radiation field, and set $G_0 = 1.7$. For the runs with different SN rates, we assume that G_0 scales linearly with the SN rate, since the main contributions to the strength of the UV radiation field comes from the same massive stars that will ultimately explode as SNe. For simplicity, in this first set of runs we take G_0 to be spatially constant.

2.4 Self-gravity

We solve Poisson's equation

$$\Delta \Phi = 4\pi G \rho \quad (25)$$

with a tree-based algorithm developed by R. Wünsch, which is part of the FLASH 4 release. It is a Barnes-Hut type octal-spatial tree (Barnes & Hut 1986) described in detail in Wünsch et al., in preparation. However, our implementation employs several modifications to this algorithm, which we briefly describe here.

We use the tree to calculate the gravitational potential and also use the information stored in it to model the attenuation of the ISRF, as described in Section 2.3 above. Since both the calculation of the gravitational potential and that of the attenuation of the ISRF share the same tree walk, the overhead costs of the latter are minimal. Moreover, the AMR grid used in our simulations is already organized into an octal tree allowing a further increase of the code efficiency by making use of the existing data structures.

Our implementation of the tree uses only monopole moments, i.e. it stores total masses, masses of H₂ and CO components and mass centre positions of the tree nodes. Therefore, to reach a specified accuracy when computing the gravitational potential, a larger number of tree nodes have to be taken into account than in the case of using quadrupole or higher order moments. However, the oct-tree with monopole moments can be constructed in an extremely memory efficient way and consequently, computational costs are spared due to efficient cache usage and faster network communication (Springel 2005; Wetzstein et al. 2009).

In this work, a GADGET2-style multipole acceptance criterion (MAC; see Springel 2005) is used to decide whether a contribution of a given node to the gravitational potential or to the column density is accurate enough, or whether children of the node should be opened. The node is accepted if

$$D^4 > \frac{GMh^2}{\Delta a_p}, \quad (26)$$

where D is the distance between the cell where the potential and the column density are calculated (target cell) and the mass centre of the tree node, h is the node size (edge of the corresponding cube), M is the node mass, G is the gravitational constant and Δa_p is the estimated error in the gravitational acceleration produced by the contribution from the node. Controlling the code accuracy by setting Δa_p is not as safe as criteria introduced by Salmon & Warren (1994) that allow control of the total error in gravitational acceleration, resulting from contributions of all nodes. However, Springel (2005) shows that the worst-case errors, resulting from situations when the target cell is inside the contributing node, can be avoided by introducing an additional criterion that does not allow the target cell lie within a volume of the node increased by a certain factor, η_{SB} . Here we follow this approach, setting $\eta_{\text{SB}} = 1.2$.

Communicating the whole tree to all processors would lead to prohibitively high bandwidth and memory requirements. Therefore, only the top part of the tree, between the root node and the nodes, which correspond to leaf blocks of the AMR grid, is communicated globally. Lower tree levels, between AMR leaf blocks and individual grid cells, are communicated only to processors where they are needed during the tree walk. Parts of the tree that need to be communicated are determined by traversing the tree for block centres only and evaluating the MAC. After that, the main tree walk proceeds by traversing the tree in a simple 'depth-first' way, running independently on each processor for all local grid cells. This part of the algorithm typically uses the majority of computational time and since it does not include any communication the code reaches almost linear scalability up to at least 2048 processors Wünsch et al., in preparation.

During the tree walk, the gravitational potential is calculated by the modified Ewald method (Ewald 1921; Klessen 1997). In order to take into account contributions of an infinite number of periodic copies of each tree node efficiently, the node contribution to the gravitational potential is split into a short-range and a long-range part ($GM/D = GM_{\text{erf}}(\alpha D)/D + GM_{\text{erfc}}(\alpha D)/D$) with α being a number between 0 and 1. The Ewald method utilizes the fact that the sum over all periodic node copies of the first term converges rapidly in physical space, while the sum of the second term converges rapidly in Fourier space. Since in our setup, the periodic node copies exist only in two directions (we use mixed boundary conditions which are periodic in x and y , but not in the z -direction), the standard equations of the Ewald method were modified by calculating analytically the limit of the periodic box size in the third (isolated) direction going to infinity, taking into account an increasing number of wave-numbers in that direction. The appropriate equations are given in Wünsch et al., in preparation.

3 SIMULATION SETUP

3.1 Gas distribution

We choose a box size of 500 pc × 500 pc × ±5 kpc. Our initial conditions are motivated by a typical galactic disc at low redshift with solar neighbourhood properties. In particular, we study a gas

Table 1. List of simulation properties. Column 1 gives the symbol and colour used to denote the run in future plots, and column 2 gives the name of the run. In column 3, we list the SN rate per Megayear. The SNe are distributed with a certain fraction of random locations, f_{RAND} , which is listed in column 4. $f_{\text{RAND}} = 1.0$ corresponds to 100 per cent random driving, whereas $f_{\text{RAND}} = 0.0$ corresponds to 100 per cent peak driving. Column 5 gives the scaling for the background UV field following the notation of Habing (1968). In column 6, we highlight specific properties.

Symbol	Sim name	SN rate (Myr $^{-1}$)	f_{RAND}	G_0 (Habing field)	Comment
●	S10-KS-rand-nsg	15	1.0	1.70	No self-gravity, random SNe
▲	S10-lowSN-rand	5	1.0	0.56	Random SNe
▲	S10-lowSN-peak	5	0.0	0.56	Peak SNe
▲	S10-lowSN-mix	5	0.5	0.56	Mixed SNe
●	S10-KS-rand	15	1.0	1.70	Random SNe
●	S10-KS-peak	15	0.0	1.70	Peak SNe
●	S10-KS-mix	15	0.5	1.70	Mixed SNe
■	S10-highSN-rand	45	1.0	5.10	Random SNe
■	S10-highSN-peak	45	0.0	5.10	Peak SNe
■	S10-highSN-mix	45	0.5	5.10	Mixed SNe
●	S10-KS-clus2	15	1.0	1.70	Clustered Type II SNe
●	S10-KS-clus	15	1.0	1.70	Clustered Type II SNe + Type Ia
●	S10-KS-clus-mag3	15	1.0	1.70	$B_0 = 3 \mu\text{G}$, clustered Type II SNe + Type Ia

surface density of $\Sigma_{\text{GAS}} = 10 \text{ M}_\odot \text{ pc}^{-2}$. We choose an SN rate in agreement with the KS relation for this surface density (see Section 3.3) and adjust the strength of the ISRF accordingly. The main parameters are explained below and summarized in Table 1.

At $t = 0$, we use a Gaussian profile to model the gaseous disc density distribution in the vertical direction:

$$\rho(z) = \rho_0 \exp \left[- \left(\frac{z}{h_z} \right)^2 \right]. \quad (27)$$

Thus, two parameters constrain the initial gas density profile, the scaleheight of the gas disc, $h_z = 60 \text{ pc}$, and the surface density, Σ_{GAS} , or equivalently, the mid-plane density $\rho_0 = 9 \times 10^{-24} \text{ g cm}^{-3}$. The Gaussian distribution is cut off at the height at which the disc density is equal to the uniform background density of $\rho_b = 10^{-27} \text{ g cm}^{-3}$, i.e. at $|z| \approx 240 \text{ pc}$. The resulting total gas mass in the disc is $M_{\text{disc}} = 2.5 \times 10^6 \text{ M}_\odot$. The initial temperature within the gas disc is set to 5000 K. In magnetic runs, we initialize the field in x -direction as

$$B_x(z) = B_{x,0} \sqrt{\rho(z)/\rho_0}, \quad (28)$$

where the magnetic field in the mid-plane is initialized to $B_{x,0} = 3 \mu\text{G}$. The fiducial resolution close to the disc mid-plane is 3.9 pc corresponding to 128 cells in x - and y -direction. In z -direction, we reduce the resolution by a factor of 2 above $|z| = 2 \text{ kpc}$.

3.2 External gravitational potential

In the MHD equations, both the gravitational acceleration due to stars and due to the gas self-gravity are included as source terms. The gravitational acceleration due to the stellar component in the galactic disc, $g_{\text{ext}}(z)$, is modelled with an external potential. We use an isothermal sheet, originally proposed by Spitzer (1942), in which the distribution function of stars is Maxwellian. The vertical density distribution then has the functional form

$$\rho_*(R, z) = \rho_*(R, 0) \operatorname{sech}^2(z/2z_d), \quad (29)$$

where R is the radial distance to the galactic centre, z is the height above the disc, and z_d is the vertical scaleheight of the stellar disc.

The mid-plane density $\rho_*(R, 0)$ is related to the surface density $\Sigma_*(R)$,

$$\rho_*(R, 0) = \frac{\Sigma_*(R)}{4z_d}. \quad (30)$$

For our setups, we choose a stellar surface density of $\Sigma_* = 30 \text{ M}_\odot \text{ pc}^{-2}$ and a vertical scaleheight of $z_d = 100 \text{ pc}$.

We solve Poisson's equation to compute the gravitational potential of the stellar disc from

$$\Delta \Phi_* = 4\pi G \rho_*. \quad (31)$$

The gravitational acceleration caused by the stars is then found from

$$g_{\text{ext}}(z) = - \frac{\partial \Phi_*}{\partial z}. \quad (32)$$

3.3 SN treatment

3.3.1 SN feedback and positioning

We model an SN event by injecting thermal energy into a spherical injection region with radius R_{inj} . The radius R_{inj} is adjusted at runtime, such that it contains a given gas mass, M_{inj} . This means that $R_{\text{inj}} \geq 4 \Delta x$ can increase freely, where Δx is the cell size on the highest refinement level.

For a single explosion, we add a thermal energy of $E_{\text{SN}} = 10^{51} \text{ erg}$. We typically use $M_{\text{inj}} = 800 \text{ M}_\odot$ for single SNe, which roughly corresponds to a star formation efficiency of ~ 8 per cent for a Chabrier initial stellar mass function (IMF; Chabrier 2001). In a low-density environment ($n \lesssim 10 \text{ cm}^{-3}$), this implementation results in a typical temperature of $\gtrsim 5 \times 10^6 \text{ K}$ within the injection regions with $R_{\text{inj}} \gtrsim 15.6 \text{ pc}$ (which corresponds to a minimum of four cells in radius), $M_{\text{inj}} \approx 800 \text{ M}_\odot$ and $E_{\text{inj}} = 10^{51} \text{ erg}$. This temperature is well above the local minimum in the cooling curve at high temperatures at a few $\times 10^5 \text{ K}$ (see e.g. Dalgarno & McCray 1972). The (momentum-generating) Sedov–Taylor phase of SNe which explode in such low-density environments is

therefore resolved and we add E_{inj} in the form of thermal energy (see equation 5):

$$\dot{u}_{\text{inj}} = \rho \frac{E_{\text{inj}}}{M_{\text{inj}}} \frac{1}{\Delta t}. \quad (33)$$

In a high-density environment ($n \gtrsim 100 \text{ cm}^{-3}$; see e.g. Walch & Naab 2015) the condition that $R_{\text{inj}} \geq 4 \Delta x$ can typically not be met with $M_{\text{inj}} = 800 M_{\odot}$. Instead, the M_{inj} will be higher in high-density environments. Therefore, the initial Sedov–Taylor expansion of the blast wave cannot be resolved and we switch to momentum input scheme as described in Gatto et al. (2015). In this case, we compute the momentum input at the end of the Sedov–Taylor phase for the mean density that is found within the injection region (Blondin et al. 1998). We then distribute this momentum evenly over all cells within the injection region leading to an effective $\dot{q}_{\text{inj}} > 0$ for these cells. In addition, the cells are heated to 10^4 K . At each SN event the global time step can be reduced according to a modified CFL criterion using the maximum of the global sound speed or velocity to determine the global time step.

We do not follow the formation of massive stars or star clusters self-consistently but choose a constant SN rate, which is informed by observations (see Section 3.3.2). Given a certain SN rate, we generate and tabulate one random sequence of SN positions at given explosion times *before* the start of the simulation. This sequence is read in upon start-up. The advantage of this approach is that it enables us to accurately compare different physics models e.g. simulations without self-gravity or with additional magnetic fields, without the bias of having different star formation and therefore SN rates and positions in the respective runs. For simulations with peak driving, the SN rate is still the same. However, each SN explodes at the position of the global density maximum at the given time.

The SNe are positioned in four different ways (see Fig. 1), where the different positioning of the SNe allows us to mimic explosions of massive stars that are still embedded within their parental molecular cloud as well as the explosion of massive stars in evolved, gas-poor environments or runaway O-stars, respectively. We use

(i) *Random driving*: the SNe are randomly distributed so as to follow a Gaussian distribution with a scaleheight of 50 pc (Tammann, Loeffler & Schroeder 1994). We only consider Type II SNe in this case.

(ii) *Peak driving*: the Type II SNe are positioned on local peaks in the density field.

(iii) *Mixed driving*: their locations are a mix of random and local peak positions, where f_{RAND} is the ratio of random SNe to the total number of SNe. $f_{\text{RAND}} = 1.0$ corresponds to purely random SN driving, and $f_{\text{RAND}} = 0.0$ corresponds to pure peak driving. We use $f_{\text{RAND}} = 0.5$ throughout this paper.

(iv) *Clustered random driving*: here, we consider the temporal and spatial correlation of Type II SNe as they stem from massive stars, which are born in associations or clusters. Each cluster has a pre-defined position and a constant lifetime of 40 Myr (Oey & Clarke 1997), and the total number of SNe per cluster, $N_{\text{SNe,clus}}$, are drawn from a truncated power-law distribution $f(N_{\text{SNe,clus}}) = N_{\text{SNe,clus}}^{-2}$ (Clarke & Oey 2002) with a lower limit of $N_{\text{SNe,clus}} = 7$ and an upper limit of $N_{\text{SNe,clus}} = 40$. Within a given cluster, the time between individual SN explosions is set to $\Delta t_{\text{SN,clus}} = 40 \text{ Myr}/N_{\text{SNe,clus}}$. We run several different simulations featuring clustered random driving.

(a) In runs denoted with ‘*clus*’, 80 per cent of all SNe are of Type II with a scaleheight of 50 pc, whereas 20 per cent are Type Ia’s with a scaleheight of 325 pc (similar to the setup used in Joung &

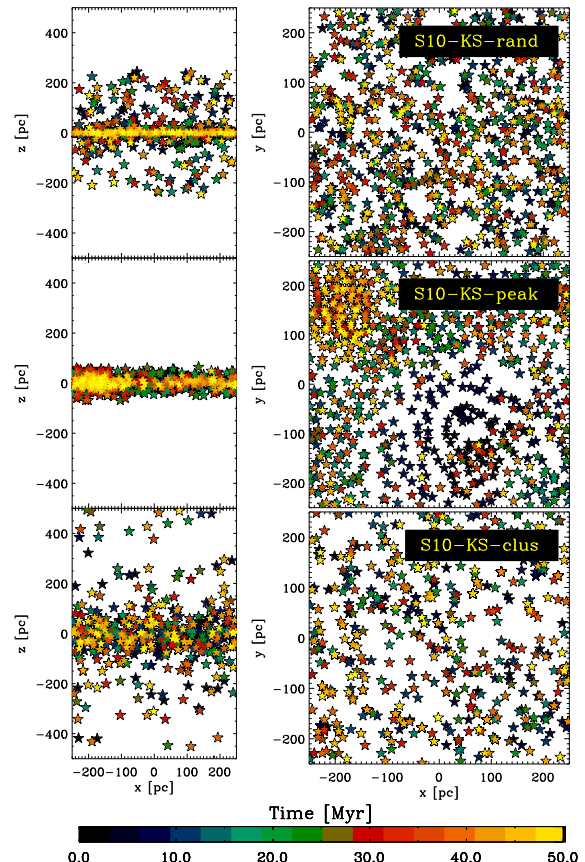


Figure 1. Distribution of SN events within the first 50 Myr (see colour code) for (i) random driving in x - z -projection and in x - y -projection (top panels); (ii) peak driving (centre); and (iii) clustered driving including Type Ia’s (bottom panels).

Mac Low 2006; Hill et al. 2012). 60 per cent of the Type II SNe are assumed to explode in clusters, and 40 per cent are single SNe exploding at random positions. In this case, to keep the overall SN rate constant at the required value, we first determine the type of each explosion (Type Ia, Type II in a cluster, or Type II at a random position), and then choose the current SN position accordingly. If the type is of ‘Type II SN in a cluster’, we find the cluster with the smallest time difference between the current simulation time and the formation time of the cluster plus $\Delta t_{\text{SN,clus}}$. If no suitable cluster is available we create a new one. Otherwise, new clusters are created when an existing one has set off all its SNe after 40 Myr.

(b) In runs denoted with ‘*clus2*’, all SNe are of Type II (as in cases i–iii) with a scaleheight of 50 pc. However, all SNe are associated with a cluster, which leads to a more coherent spatial distribution.

3.3.2 SN rates

Since we do not follow star formation self-consistently, we have to choose an SN rate for our simulations. For this reason, we compile all popular scaling relations of Σ_{SFR} versus Σ_{GAS} , which have been inferred from observations, in Fig. 2. These are (i) the Kennicutt–Schmidt (KS) relation (Kennicutt 1998) with $\Sigma_{\text{SFR}} \propto \Sigma_{\text{H}_2 + \text{HI}}^{1.4}$, as well as (ii) newer results which relate the SFR surface density to the

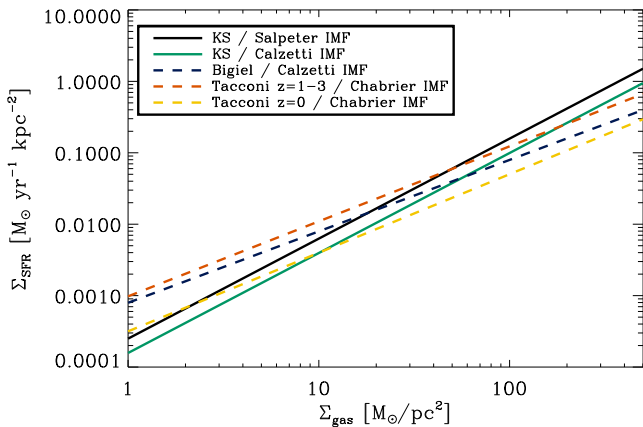


Figure 2. A compilation of proposed power-law scaling relations of the SFR surface density, Σ_{SFR} , versus total gas surface density, $\Sigma_{\text{H}_2+\text{HI}}$ (full lines), or molecular mass surface density, Σ_{H_2} (dashed lines), respectively. The scaling relations of Σ_{SFR} versus $\Sigma_{\text{H}_2+\text{HI}}$ follow a power-law index of 1.4. The offset depends on the underlying stellar IMF. Here, we show two possibilities: (1) black line: the standard KS relation (Kennicutt 1998) as derived for a Salpeter IMF (Salpeter 1955), and (2) green line: the KS relation scaled with the IMF from Calzetti et al. (2007), which is the standard IMF in STARBURST99 (Leitherer et al. 1999). The scaling relations of Σ_{SFR} versus Σ_{H_2} are approximately linear. We show the results of (3) blue line: Bigiel et al. (2008), who use the same IMF as (2); (4) red line: Tacconi et al. (2013), their fit to high-redshift galaxies, and (5) yellow line: Tacconi et al. (2013), their fit to low-redshift galaxies, both of which assume a Chabrier IMF (Chabrier 2003).

molecular gas surface density, Σ_{H_2} , in a galaxy in a linear fashion³ (Bigiel et al. 2008; Tacconi et al. 2013). Please note that Σ_{GAS} (as plotted on the x -axis in Fig. 2) may therefore be equal to $\Sigma_{\text{H}_2+\text{HI}}$ or Σ_{H_2} depending on which line one refers to. In any case, Σ_{H_2} should approach $\Sigma_{\text{H}_2+\text{HI}}$ for high gas surface densities, where basically all gas is in molecular form. We argue that according to Fig. 2 a factor of 3 uncertainty in Σ_{SFR} for any given Σ_{GAS} can easily be justified.

We then translate Σ_{SFR} into an SN rate by assuming a standard IMF (Chabrier 2001), which implies that approximately one massive star forms for every 100 M_\odot of gas that is turned into stars. Now scaling this value to our simulated volume results in a standard (KS) SN rate of 15 Myr^{-1} for $\Sigma_{\text{GAS}} = 10 \text{ M}_\odot \text{ pc}^{-3}$ (see Table 1). We test the influence of the SN rate on the resulting ISM distribution by also performing simulations with a three times lower and three times higher SN rate (*lowSN* and *highSN* runs). The ISRF is linearly correlated with the SFR (see Section 2.3) and therefore it is changed accordingly in the simulations (see Table 1).

4 FIDUCIAL SET OF RUNS

In our six fiducial models, we study the evolution of a stratified disc with $\Sigma_{\text{GAS}} = 10 \text{ M}_\odot \text{ pc}^{-3}$, which is driven by randomly placed or clustered SNe at a rate of 15 Myr^{-1} , which corresponds to the KS value. Initially, the disc is represented by a Gaussian gas density distribution in the vertical direction. The disc gas is initialized as atomic hydrogen (see Fig. 3). When starting the simulation, the gas collapses towards the mid-plane due to the external gravitational

³ Recently, using Bayesian linear regression, Shetty, Kelly & Bigiel (2013) have pointed out that the relation might actually be sublinear. For simplicity, we do not consider this here.

potential. At the same time, it is stirred by SN-driven turbulence until a complex, multiphase ISM emerges. In particular, we compare runs

1. *S10-KS-rand-nsg*: without self-gravity and random driving;
2. *S10-KS-rand*: the standard run with random driving;
3. *S10-KS-peak*: using peak driving;
4. *S10-KS-mix*: using mixed driving with $f_{\text{RAND}} = 0.5$;
5. *S10-KS-clus2*: using clustered Type II SNe. Clusters are distributed randomly following a Gaussian distribution in z -direction with a scaleheight of 50 pc.
6. *S10-KS-clus*: using ~ 50 per cent of clustered Type II SNe, ~ 30 per cent of random Type II SNe with a scaleheight of 50 pc, and 20 per cent Type Ia SNe with a larger scaleheight;
7. *S10-KS-clus-mag3*: MHD run with clustered SN driving.

This set of simulations represents a sequence of runs with increasing physical complexity. As an additional branch, the influence of the SN positioning (random/peak/mix/clustered) is explored.

We also perform runs with lower and higher SN rates. These are discussed later on (see section 5). In Table 1, we list all of the runs and their properties.

4.1 Example: evolution of run *S10-KS-rand*

In Fig. 4, we show run *S10-KS-rand* at $t = 50$ and 100 Myr . From left to right, we plot slices of the density (in the x - z -plane and in the disc mid-plane), the column density, slices of the gas temperature, and column densities of ionized hydrogen, atomic hydrogen, molecular hydrogen, and CO. The gas density and temperature distributions span a large dynamic range. Most of the cold gas is located close to the disc mid-plane, where multiple molecular clouds, which are visible in H_2 and CO, are forming and evolving. As time goes on, the clouds evolve continuously and do not come into an equilibrium configuration. They collide, merge, and are pushed by nearby SN explosions, thereby picking up bulk motion and angular momentum. The total CO mass fraction and the total H_2 mass fraction evolve in a similar way in all simulations (see Section 4.3). However, CO shows larger fractional variations than H_2 . CO is embedded within H_2 clumps at high column densities and thus, does not trace all of the H_2 within a particular clump (see Smith et al. 2014, for a detailed analysis on galactic scales). Furthermore, within the dense gas self-gravity is locally important (see Section 4.4 for a further discussion).

A large fraction of the ISM is filled with hot gas, which is injected in the SN explosions. The hot gas is nicely visible in the H^+ component, which is dominated by thin filaments and bubbles, which are particularly apparent in the disc mid-plane. Outflowing gas is lifted off the disc, mostly in the form of atomic hydrogen. The bulk of this material moves with velocities of $\sim 10 \text{ km s}^{-1}$ (at maximum, with the sound speed of the respective gas component) and consequently reaches a distance of $\sim 1 \text{ kpc}$ after $\sim 100 \text{ Myr}$. Since the gas velocity is smaller than the escape velocity of this galaxy, it is expected to return and thus, form a galactic fountain. The galactic outflow rates and the multiphase structure of the outflow are discussed in a companion paper (Girichidis et al. 2015, hereafter *SILCC2*).

4.2 Comparison: qualitative evolution of all fiducial runs

We plot the disc structure for run *S10-KS-rand-nsg* at $t = 50$ and 100 Myr in Fig. 5; for run *S10-KS-clus2* at $t = 50$ and 100 Myr in

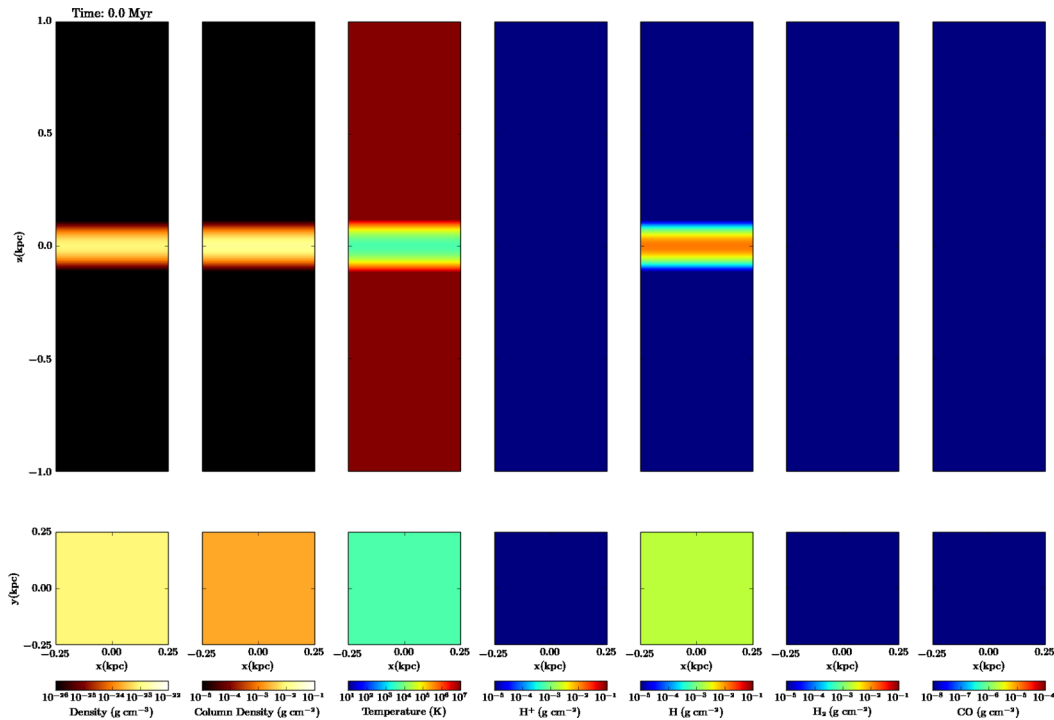


Figure 3. Initial conditions for all runs around the disc mid-plane. From left to right: gas density (slice), column density (projection), gas temperature (slice), and column densities of H^+ , H and H_2 , and CO . All slices are taken at $y = 0$ (top panels), or at $z = 0$ (bottom panels), respectively. Accordingly, the column density is projected along the y - or z -axis.

Fig. 6; for run *S10-KS-clus-mag3* at $t = 50$ and 100 Myr in Fig. 7; for run *S10-KS-peak* at $t = 50$ and 100 Myr in Fig. 8; and for run *S10-KS-mix* at $t = 50$ and 100 Myr in Fig. 9.

Compared with *S10-KS-rand*, the run without self-gravity (*S10-KS-rand-nsg*) shows a disc structure which is less concentrated to the disc mid-plane. Consistently, also the larger scale structure and the developing outflow appear more extended. There is molecular gas present, but there seems to be less of it, in particular less CO (see Section 4.3 for a more quantitative analysis). Also, the structures traced by molecular hydrogen are more extended (fuzzy).

In run *S10-KS-clus2* with clustered SN driving, we can see the opposite effect. Compared with *S10-KS-rand*, there is a bit more molecular gas and the disc is much more concentrated to the mid-plane with less mass in atomic hydrogen being entrained in the outflow. Although there are a few molecular clumps at $t = 50$ Myr, there is only one main molecular cloud left towards the end of the simulation at $t \approx 100$ Myr. Thus, with clustered instead of random driving, the clouds seem to merge more rapidly. With a fraction of the SNe in a more extended Type Ia component and additional magnetic fields (run *S10-KS-clus-mag3*; Fig. 7), we see a very similar evolution of the molecular clumps as in *S10-KS-clus2*. However, the outflow is less asymmetric, similar to run *S10-KS-rand*.

With peak driving the discs are highly concentrated to the mid-plane. All components have a small scaleheight and there is no outflow developing. The top-down view in Fig. 8 shows a less clumpy and more filamentary distribution of the dense gas. For peak driving, there is little H_2 and basically no CO present throughout the simulation.

The mixed driving case (Fig. 9) shows an intermediate ISM structure with respect to peak and random driving. Some molecular

clouds form in the disc mid-plane and merge towards the end of the simulation at 100 Myr. The outflow develops a bit more slowly and the ISM is slightly more diffuse than in case of random driving.

4.3 Chemical evolution of the discs

In Fig. 10, we show the total mass fractions in atomic hydrogen, H , molecular hydrogen, H_2 , and carbon monoxide, CO , as a function of time. The atomic and molecular hydrogen mass fractions are shown with respect to the total hydrogen mass. For CO , we instead show the fraction of the total mass of carbon that is in the form of CO rather than C^+ . Overall, the H distribution is roughly the inverse of the H_2 plus CO mass fractions. A further analysis shows that the mass fraction of ionized gas (not shown here) remains roughly constant at $\sim 5\text{--}10$ per cent. The total CO mass fraction evolves similar to the H_2 fraction, modulo somewhat larger fluctuations.

For run *S10-KS-rand* (black line), the H_2 mass fraction grows to ~ 40 per cent within the first 30–35 Myr. Thereafter, the evolution is rather flat and the H_2 mass fraction stays at $\sim 35\text{--}40$ per cent. The mass fraction of atomic hydrogen decreases and increases inversely proportionally to H_2 .

Comparing the different runs, we see that self-gravity significantly changes the structure of the dense interstellar medium and, therefore, should not be neglected in studies of stratified galactic discs. Without self-gravity (yellow line; see also Gatto et al. 2015), compared to all other simulations, the molecular gas mass fractions are reduced to a minimal amount of ~ 3 per cent at late times, whereas ~ 90 per cent of the mass is in atomic gas. Consequently, ~ 7 per cent of the total mass is in ionized hydrogen.

Only in the case of peak driving (green lines) do we find even less H_2 . Since 100 per cent of the SNe interact with dense gas in

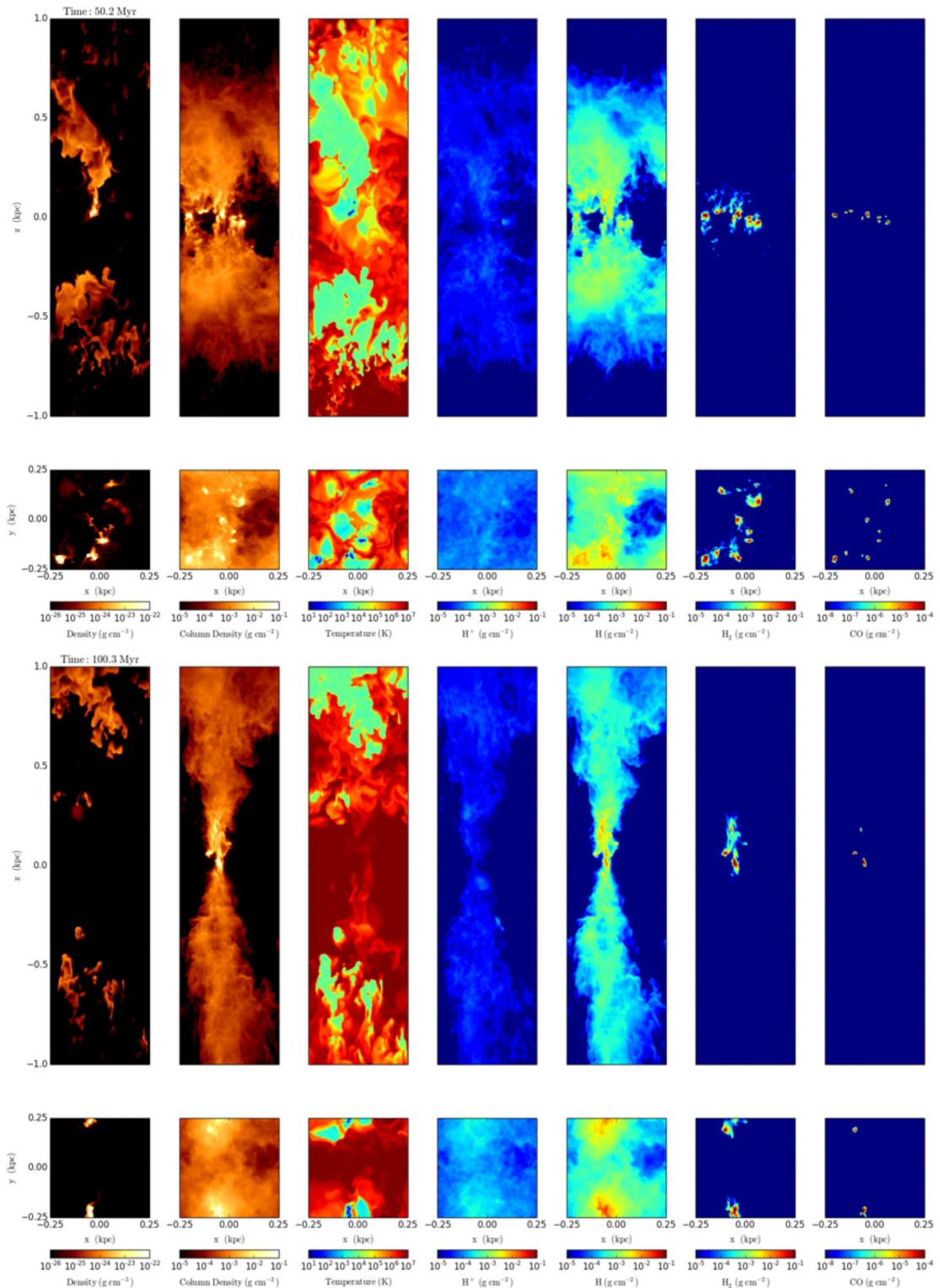


Figure 4. Snapshot of run *S10-KS-rand* at $t = 50$ Myr (top) and at $t = 100$ Myr (bottom). Only a section of the simulation box, which measures $0.5 \text{ kpc} \times 0.5 \text{ kpc} \times 2 \text{ kpc}$, is shown. From left to right: gas density (slice), column density (projection), gas temperature (slice), and column densities of H^+ , H and H_2 , and CO . All slices are taken at $y = 0$ (elongated panels), or at $z = 0$ (square panels), respectively. Accordingly, the column density is projected along the y - or z -axis.

this case, H_2 is locally dissociated and the dense molecular clouds are dispersed. Employing peak driving leads to the establishment of a dynamical equilibrium in the disc, since the dense gas is efficiently dispersed and therefore not locked up into dense clouds.

Nevertheless, we believe that peak driving at a fixed SN rate is not a good way to model feedback in galactic discs as it fails to reproduce the observed structure of the multiphase ISM (e.g. almost no H_2 present). Also, a significant delay of a few million

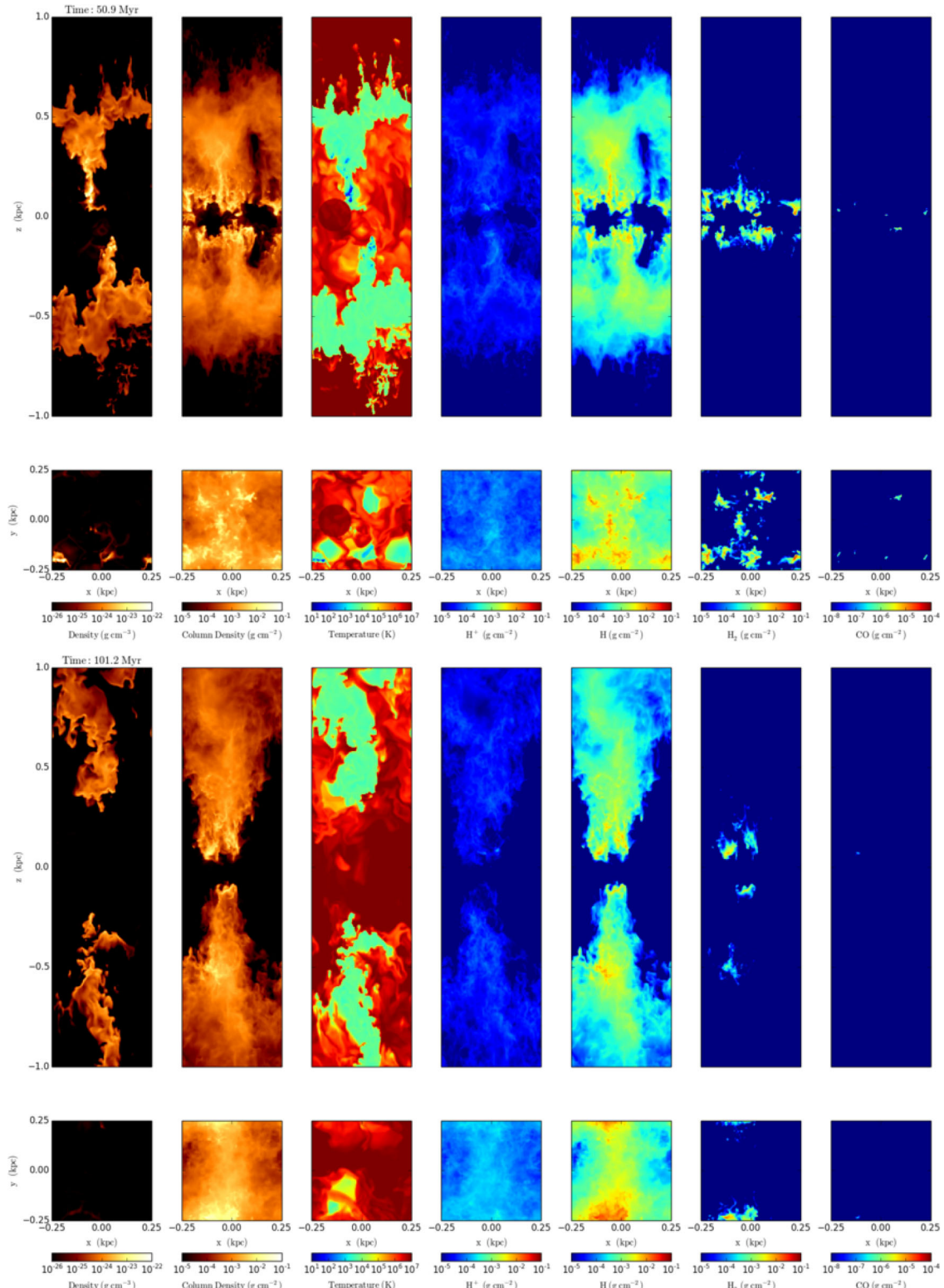


Figure 5. Same as Fig. 4 but for run *S10-KS-rand-nsg* without self-gravity at $t = 50$ Myr (top) and at $t = 100$ Myr (bottom).

years between the formation of a massive star and its SN explosion would decouple the explosions from the densest peaks, leading to a different positioning of the SNe with respect to the dense gas. Therefore, a regulation of the SFR by SN feedback alone seems artificial.

How effective the gas dispersal by SNe is, depends on the SN rate (see Section 5) as well as on the mean density of the gas within which the SN explodes. If the mean density becomes too high, i.e. the mean density is $\bar{n} \gtrsim 10^3 \text{ cm}^{-3}$, then the SN remnants quickly become radiative (Blondin et al. 1998; Gatto et al. 2015; Li et al.

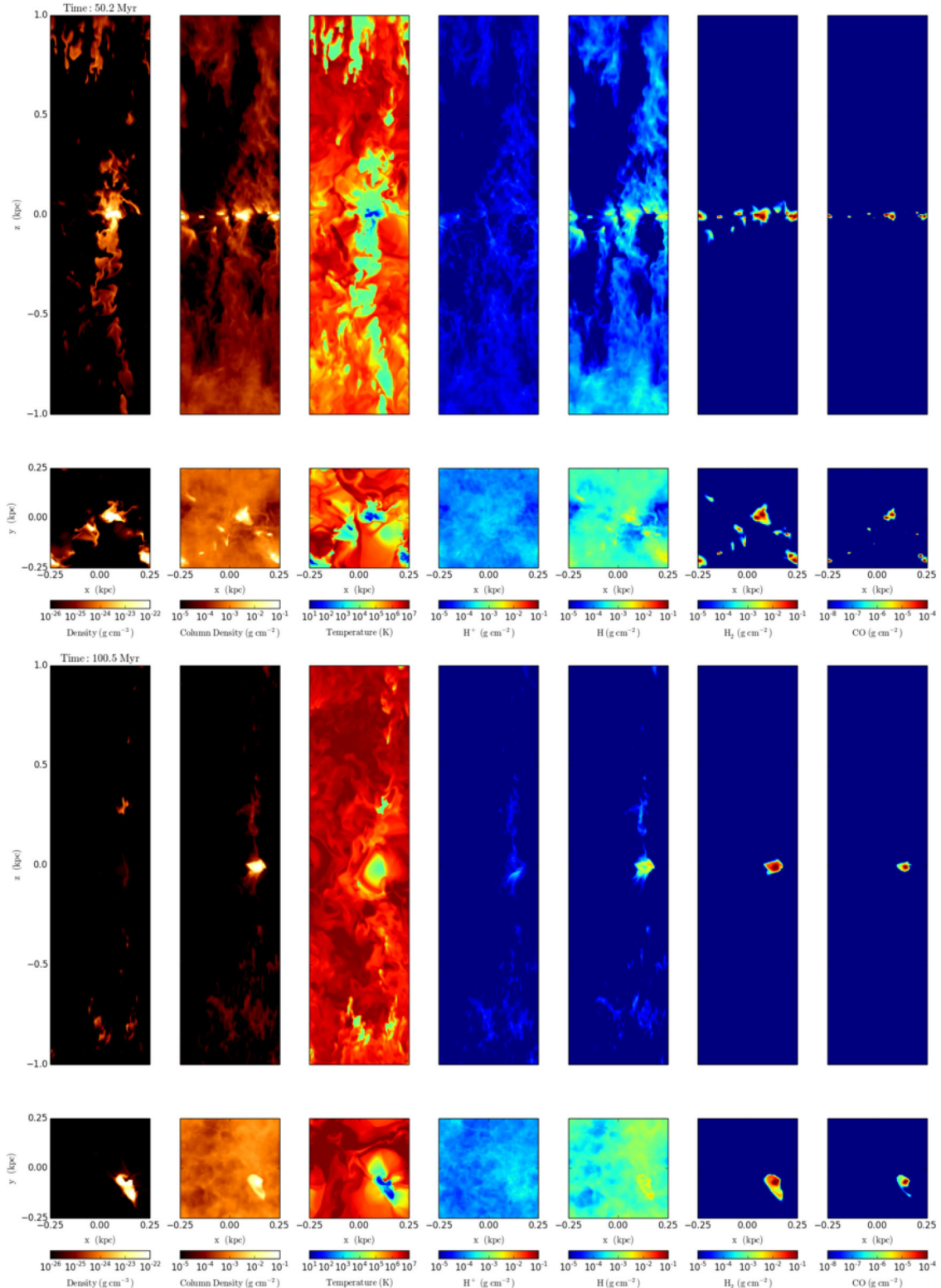


Figure 6. Same as Fig. 4 but for run S10-KS-clus2 with clustered SN driving at $t = 50$ Myr (top) and at $t = 100$ Myr (bottom).

2015) and the leftover momentum input ($\sim 3 \times 10^5 M_\odot \text{ km s}^{-1}$) is not strong enough to disperse the molecular clumps. This happens in case of mixed driving (violet lines), where only 50 per cent of all SNe are interacting with dense gas and, consequently, the gas has more time to collapse to higher densities before being heated

by an SN explosion. Fig. 10 shows that the H_2 mass fraction grows more slowly for mixed driving than for e.g. random driving, but at the same time, the H_2 mass fraction continues to increase and reaches ~ 73 per cent at the end of the simulation at 100 Myr, which is the highest H_2 fraction of all simulations.

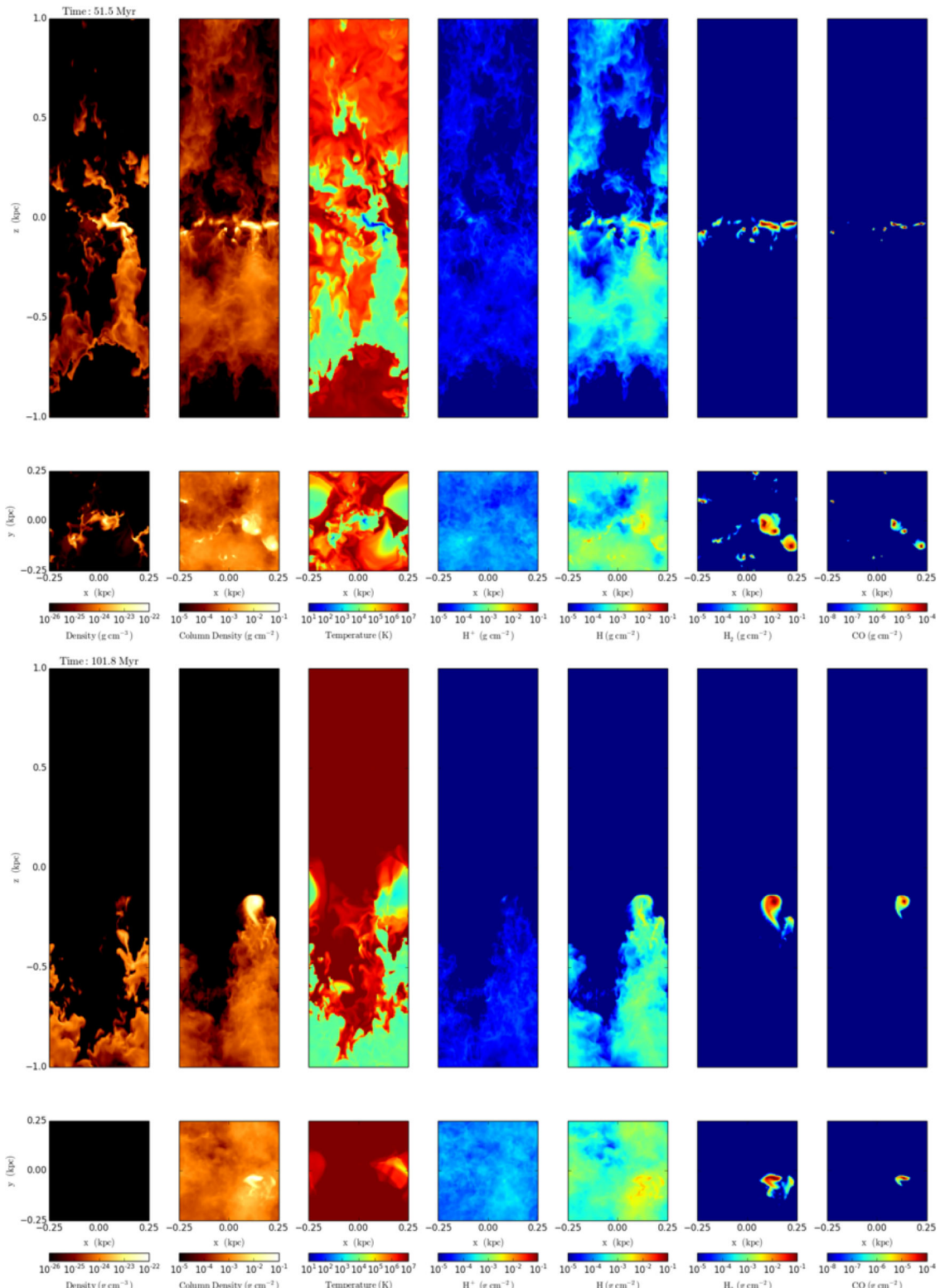


Figure 7. Same as Fig. 4 but for run *S10-KS-clus-mag3* with clustered SN driving and magnetic fields at $t = 50$ Myr (top) and at $t = 100$ Myr (bottom).

Moreover, runs with clustered SN driving and a small fraction of Type Ia SNe [with (red lines) and without magnetic fields (blue lines)], result in higher mean mass fractions of H_2 and CO than with random driving (50–60 per cent instead of 40 per cent as for run *S10-KS-rand*). With an initial magnetic field, the formation of

H_2 is delayed by ~ 20 Myr, but increases with a similar slope to the case of clustered SNe without magnetic fields once it is initiated.

The run *S10-KS-clus2* in which 100 per cent of the SNe explode in clusters, evolves similar to *S10-KS-clus*, which has an additional Type Ia component. At 100 Myr, the H_2 mass fraction in

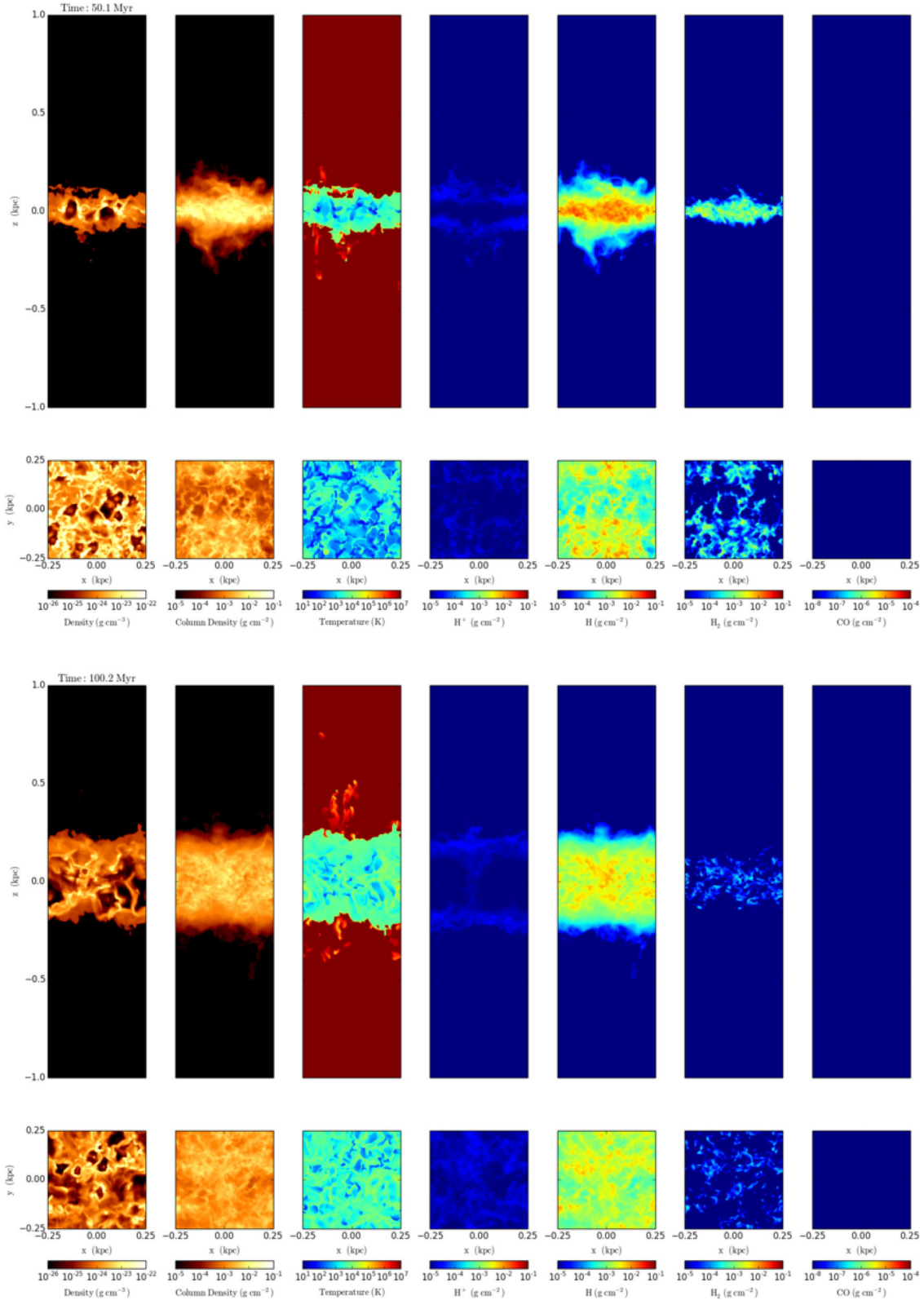


Figure 8. Same as Fig. 4 but for the run with peak driving *S10-peak-KS* at $t = 50$ Myr (top) and $t = 100$ Myr (bottom).

S10-KS-clus2 is ~ 10 per cent higher than in *S10-KS-clus*. This is probably caused by the even higher compression which is provided by the fully clustered SNe setup. The more extended Type Ia component seems to have little effect on the mass fractions.

4.4 The distribution of molecular gas

We discuss the morphology and evolution of the forming molecular gas as a function of time. Due to our limited resolution, we do not consider the CO abundance to be fully converged. Therefore, we

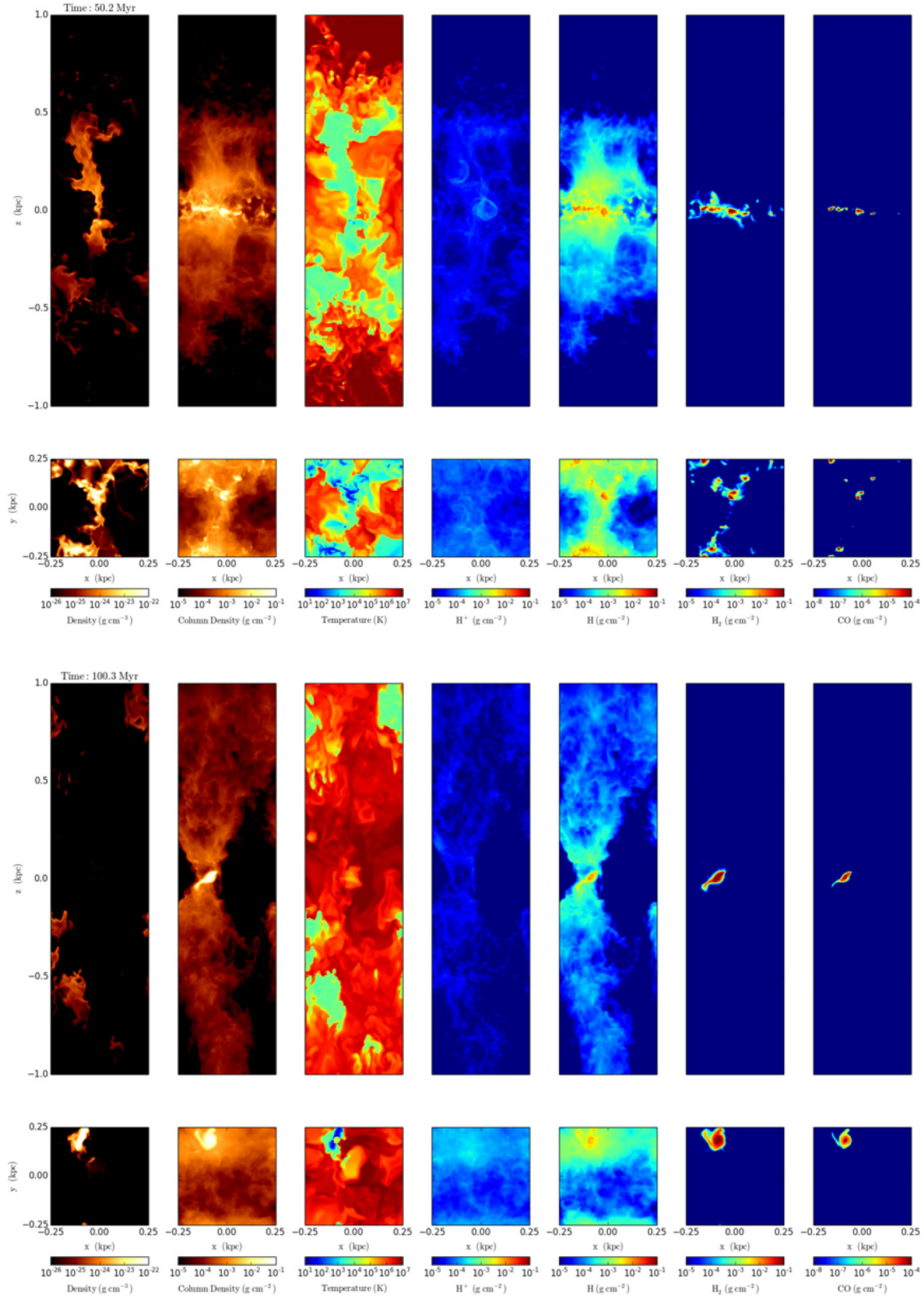


Figure 9. Same as Fig. 4 but for the run with mixed driving S10-mix-KS at $t = 50$ Myr (top) and $t = 100$ Myr (bottom).

focus on the morphology of gas in the form of H_2 . In Figs 11 and 12, we show the time evolution of the total and the H_2 surface density for runs S10-KS-rand-nsg, S10-KS-rand (Fig. 11), and S10-KS-clus2, S10-KS-clus, and S10-KS-clus-mag3 (Fig. 12).

In all simulations, the molecular gas forms in shock-compressed filaments which evolve into clumps that merge into larger clouds during the course of the simulation. Without self-gravity, the small amount of H_2 can only form in shock-compressed structures. These

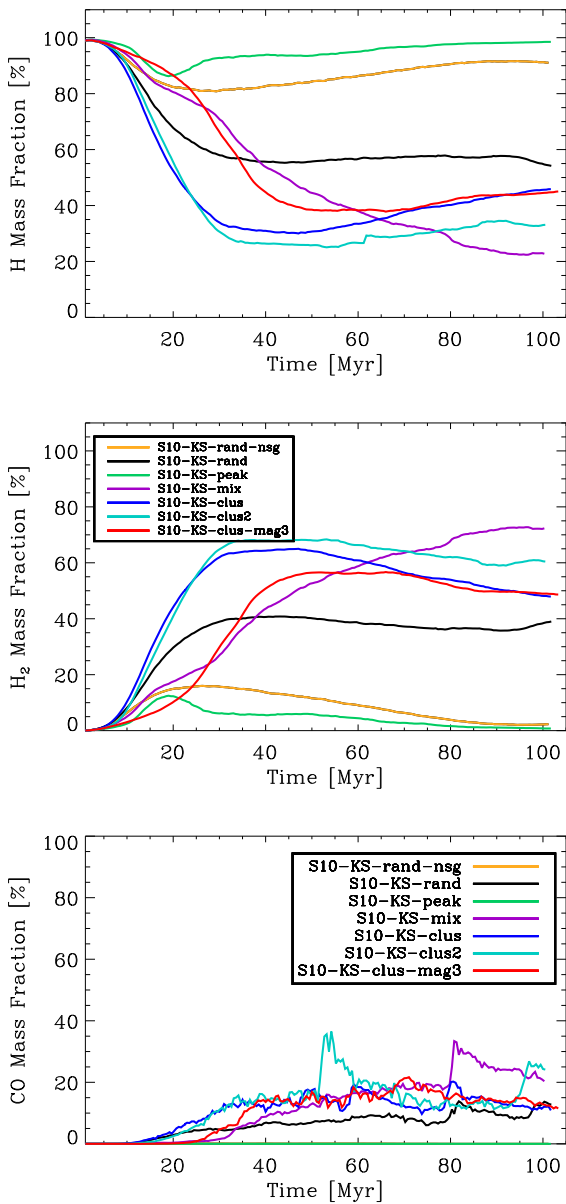


Figure 10. H (top) and H₂ (middle) mass fractions (with respect to the total hydrogen mass) and CO mass fraction (bottom; showing the fraction of carbon in the form of CO) as a function of time for all main runs with $\Sigma_{\text{GAS}} = 10 \text{ M}_\odot \text{ pc}^{-2}$ using the KS SN rate, i.e. 15 Myr^{-1} . Atomic hydrogen is roughly the inverse of H₂, modulo some 5–10 per cent of mass, which resides in the form of ionized hydrogen. The formation of CO is similar to H₂, but the time variations are stronger. H₂ grows within the first 20–40 Myr and stays roughly constant at later times. Clustered driving with/without an additional SN Type Ia component evolve similarly, although purely clustered Type II SNe result in a slightly higher H₂ mass fraction due to a higher compression. Magnetic fields delay H₂ formation. Runs without self-gravity and runs with peak driving have the smallest H₂ fraction, well below 10 per cent at $t = 100$ Myr. Mixed driving has a gentle growth of H₂ but at the same time the highest fraction at $t = 100$ Myr.

are sometimes pushed together by the SN feedback, which results in a clumpy medium. However, due to the absence of self-gravity, the clumps do not feel each others' gravitational attraction and the H₂ mass fraction saturates at a low level as the distribution comes to a dynamical equilibrium. For clustered driving (Fig. 12), larger, superbubble like dense structures develop, which contain clumpy

molecular gas. The small number of single, random SNe as well the Type Ia component in runs *S10-KS-clus* (middle panel) and *S10-KS-clus-mag3* (bottom panel) do not make a significant difference to the gas distribution with respect to run *S10-KS-clus2* (top panel), which only features clustered Type II SNe. This shows that, if present, clusters of SNe completely dominate the shaping of the dense ISM. Similar to the run without self-gravity, runs with self-gravity and additional magnetic fields (run *S10-KS-clus-mag3*) show a more diffuse gas distribution than without magnetic fields. In particular, the formation of the dense phase is hindered by additional magnetic pressure.

In Fig. 13, we show the impact of the SN positioning with respect to the dense gas on the H₂ distribution. At first, peak and mixed driving (middle and bottom rows) form more coherent, large-scale bubbles than random driving (top row). As the bubble(s) expand and collide (similar to a typical colliding flow scenario, e.g. Banerjee et al. 2009; Heitsch, Naab & Walch 2011) the H₂ distribution in case of peak driving is dispersed and becomes very filamentary. In case of mixed driving, the SN feedback is not strong enough to disperse all of the dense gas (since only every other SN is correlated with the dense gas) and molecular clouds survive. In the end, the results obtained for mixed driving seem to represent an extreme case of clustered driving with just one large-scale colliding flow. This is consistent with the large H₂ mass fraction formed in run *S10-KS-mix* (see Fig. 10). Overall this fits into the global picture that the more coherent the SN feedback is, the more it may sweep up and compress the gas. This leads to a quick conversion of atomic to molecular hydrogen once self-gravity starts to dominate locally, which in turn promotes the formation of H₂.

In Fig. 14, we show the corresponding volume-weighted density probability density functions (PDFs) for all seven fiducial runs at $t = 50$ and 100 Myr. With the exception that the non-gravitating run as well as the peak driving run both lack the high-density gas, the density PDFs are very similar and do not reflect the structural changes in the gas surface density distribution. Also, we see that a power-law tail at high densities has already been developed at $t = 50$ Myr, which confirms that the molecular clouds that populate this density regime are self-gravitating and would collapse to form stars.

5 IMPACT OF THE SFR

We decrease/increase the SN rate by a factor of 3 to mimic higher and lower SFRs in the discs (runs *S10-lowSN-rand/-peak/-mix* and *S10-highSN-rand/-peak/-mix*). The runs therefore explore the disc structure below/above the KS relation. In Fig. 15, we show the impact of the lower/higher SN rates on the vertical disc structure by means of plotting the atomic hydrogen column densities. From left to right, the SN rate increases and the driving mode is changed from peak to random driving. The vertical scaleheight of the gas clearly depends on the input SN rate, with highly concentrated distributions in case of the low SN rate, and highly puffed up (run *S10-highSN-peak*) or even completely dispersed distributions in case of high SN rates.

The face-on view of the discs as shown in Fig. 16, compares the time evolution of the gas morphology for random driving at different SN rates. In agreement with Fig. 15, we find that, with increasing SN rate (from top to bottom), the ISM becomes more diffuse. At the same time, it becomes less molecular. While multiple molecular clouds are formed in run *S10-lowSN-rand*, there is little H₂ left in run *S10-highSN-rand*. From this analysis, we may conclude that SN rates that are as high as three times the KS value could not

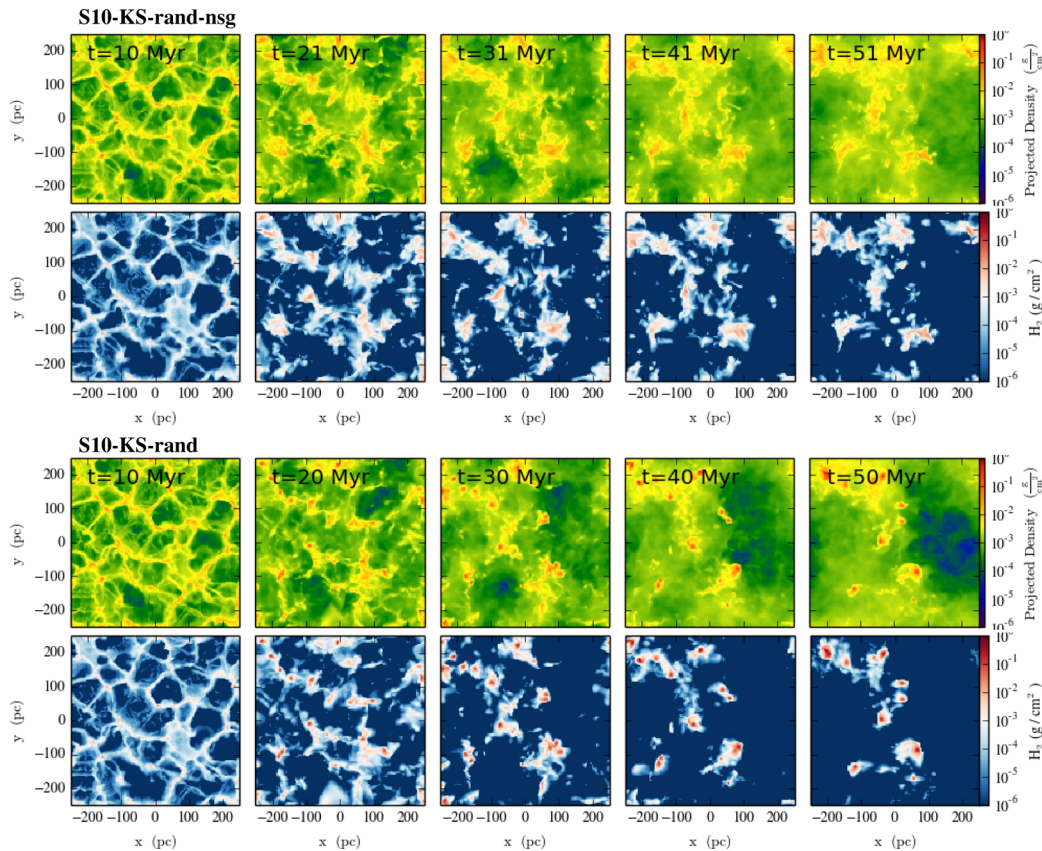


Figure 11. Time evolution of total and H_2 column densities (as seen face-on) for runs with different levels of physical complexity, i.e. *S10-KS-rand-nsg* (top) and *S10-KS-rand* (second row). Without self-gravity the molecular clouds appear to be more diffuse.

be maintained in a self-consistently star-forming ISM because all molecular gas is dispersed due to the high input of SN energy and momentum.

In Fig. 17, we quantitatively show that the molecular gas mass fractions strongly depends on the SN rate. The H_2 mass fraction is reduced from on average ~ 75 per cent in case of a low SN rate (5 Myr^{-1} ; dashed curve) to ~ 40 per cent for the KS rate (15 Myr^{-1} ; solid curve) to almost 0 per cent for the high SN rate (45 Myr^{-1} ; dash-dotted curve). The mass in H^+ is $\sim 5\text{--}10$ per cent for all simulations. The CO mass fractions show a similar trend as the H_2 mass fractions.

Interestingly, the different SN rates also have a measurable effect on the volume-weighted density PDFs, which are shown in Fig. 18 for random (black lines) and peak driving runs (green lines). For both, random and peak driving, the amount of dense gas is significantly reduced for increasing SN rates, essentially cutting off the power-law tail which consists of cells with dense, molecular gas. Therefore, the PDF of runs with a high SN rate appears more narrow than the ones derived from runs with a low or KS SN rate, which seems to be in contradiction with a simple broadening of the density and column density distributions with increasing levels of turbulence. For low SN rates, even the peak driving run shows a power-law tail, which is in agreement with the survival of molecular clumps in run *S10-lowSN-peak*.

6 VERTICAL DISTRIBUTIONS

As inferred from our analysis, the vertical distributions of the different chemical species are strongly influenced by the SN rate and

position. Higher peak fractions as well as lower SN rates lead to a vertical density distributions which is more concentrated to the disc mid-plane. In Fig. 19, we show the vertical density profiles of H^+ , H , H_2 , and CO at $t = 50$ Myr (left-hand column) and $t = 100$ Myr (right-hand column). In the central column, we plot the volume filling fractions (VFFs) as a function of the vertical height at $t = 50$ Myr. From top to bottom, we show run *S10-KS-rand-nsg* without self-gravity (top row), run *S10-KS-rand* with random driving (second row), run *S10-KS-peak* with peak driving (third row), run *S10-KS-clus2* (fourth row) with fully clustered driving, and *S10-KS-clus-mag3* (bottom row) with a partly clustered, partly random SN driving including a broader Type Ia component as well as with additional magnetic fields.

For all but run *S10-KS-peak*, the central densities are dominated by the molecular component. At larger scaleheights, above 10–30 pc, the total density profile is dominated by atomic hydrogen. Ionized hydrogen generally contributes little to the total density distribution. In some cases (run *S10-KS-clus-mag3* and run *S10-KS-rand-nsg* at 100 Myr), the profiles become asymmetric. As a function of time, the disc is destroyed in case of high SN feedback. It seems that, if magnetic fields are included, even a KS SN rate could be too high to be maintained without dispersing the disc over a time-scale of 100 Myr.

The vertical profiles confirm that the concentration of the disc towards the mid-plane is strongly influenced by the type of SN driving. The discs are thicker for random than for peak driving, which we quantify by computing the vertical height that encloses 90 per cent of the total atomic hydrogen mass in the disc (green dotted vertical lines). This measure turns out to be robust, whereas

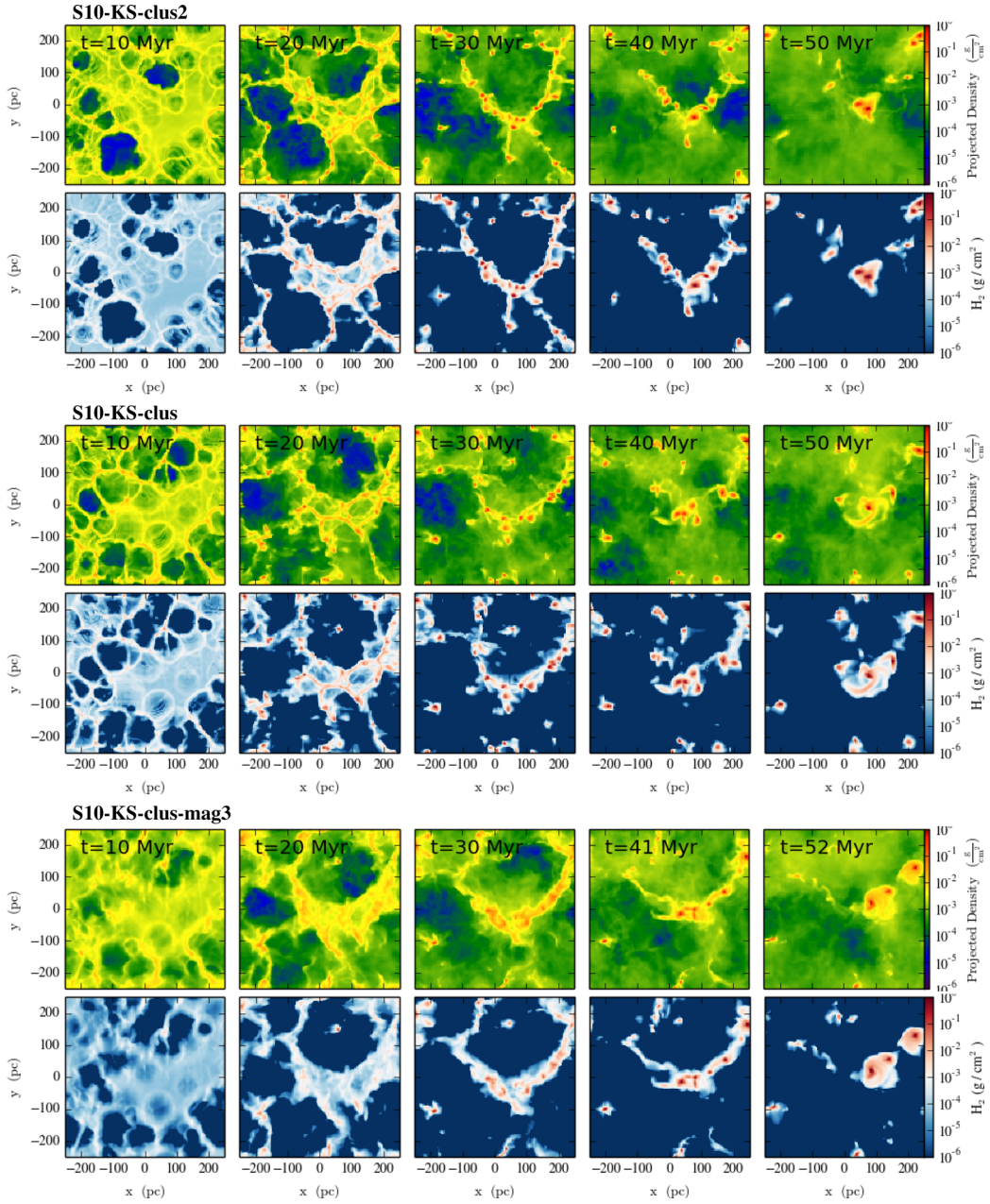


Figure 12. Fig. 11 continued. Time evolution of total and H_2 column densities for runs *S10-KS-clus2* (first row), *S10-KS-clus* (second row), and *S10-KS-clus-mag3* (bottom). The difference between fully clustered SNe (*S10-KS-clus2*) and clustered Type II SNe plus a more extended Type Ia component (*S10-KS-clus*) is small, however, in *S10-KS-clus* the clouds appear to be slightly more concentrated. With magnetic fields (*S10-KS-clus-mag3*) there are fewer clouds. These are less dense and some more diffuse H_2 is present.

we find that fitting the vertical profiles with a given function (e.g. a Gaussian) is not very educative since any choice of a Gaussian, lognormal, power law, or exponential function is possible but, at the same time, may only provide a good fit to a small part of the distribution. We list the derived values of the disc ‘scaleheight’, which encloses 90 per cent of the atomic hydrogen mass at $t = 50$ Myr in Table 2.

We point out that the H distribution is not completely different with and without self-gravity, i.e. it is not off by an order of magnitude. Therefore, gas self-gravity cannot be the main agent for setting the scaleheight of atomic hydrogen. This analysis suggests that self-gravity is rather a secondary effect for gaseous discs with

a relatively low surface density, while the global gravitational potential of these discs is dominated by the stellar population (here represented by the external gravitational potential), which mainly determines the vertical disc structure. It provides the balance for the energy and momentum input by SNe (see paper SILCC2 for a discussion on the global pressure balance and the evolution of the atomic hydrogen scaleheights).

Concerning the vertical VFF profiles of the chemical species, runs *S10-KS-rand* and *S10-KS-rand-nsg* seem to give the most realistic values for the hot, ionized and the warm, atomic ISM towards the disc mid-plane (about 50 per cent each). The peak driving runs generally produce a very high atomic hydrogen VFF (~ 95 per cent

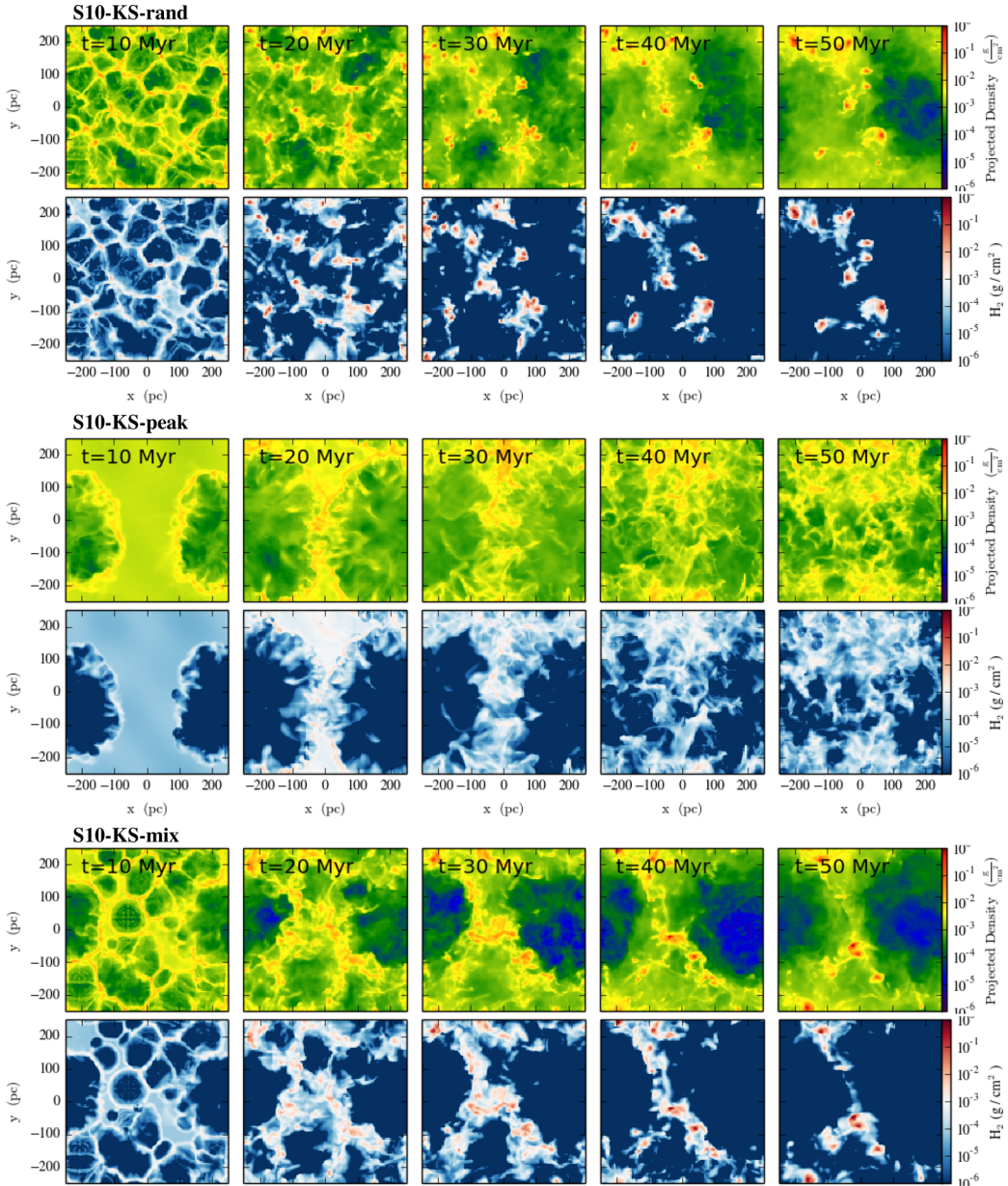


Figure 13. Time evolution of the total and H_2 column densities for runs with different SN placement, i.e. *S10-KS-rand* (top), *S10-KS-peak* (centre), and *S10-KS-mix* (bottom). The placement of the SNe strongly affects the gas distribution and thus, also the H_2 distribution and total mass fraction (see Fig. 10). Run *S10-KS-peak* looks like a classical colliding flow scenario, whereas the gas distribution in run *S10-KS-mix* is in between completely random and peak driving.

for *S10-KS-peak*), which seems inconsistent with observations of the Milky Way.

Following McKee & Ostriker (1977) and Tielens (2005), we can estimate the VFF of the hot phase that we expect for a given SN rate and mean gas density. The porosity parameter

$$Q \approx 0.12 N_{\text{SN}} \left(\frac{E}{10^{51} \text{ erg}} \right)^{-44/45} n_0^{-44/45} \quad (34)$$

is an estimate of the probability that a randomly distributed SN explodes within the bubble blown by a previous remnant. Here, N_{SN} is the SN rate within the whole galaxy per 100 yr and n_0 is the mean density of the ISM. For $n_0 = 1 \text{ cm}^{-3}$ and $N_{\text{SN}} \simeq 0.19$, which is roughly the KS SN rate of 15 Myr^{-1} scaled up to a full disc with radius 10 kpc, we derive $Q \simeq 0.228$. Note that the scaling of Q with mean density is almost linear. Therefore, $n_0 = 0.2 \text{ cm}^{-3}$ gives

$Q \simeq 1.0$, which results in $f_{\text{hot}} = Q/(1+Q) = 0.5$. This corresponds to the hot gas VFF close to the disc mid-plane for model *S10-KS-rand*. The two runs with clustered driving have higher hot gas VFFs, which is consistent with a higher spatial correlation of the SN events. However, Q can only be computed approximately since the H^+ density distribution is broad (see Section 7.1). We discuss the VFFs of different temperature phases for all runs in Section 8.

How variable is the vertical disc structure as a function of time? The answer is, highly. From the right-hand column of Fig. 19, one can see that the disc density profiles are much more extended at $t = 100$ Myr. For instance, for run *S10-KS-rand*, the 90 per cent atomic hydrogen scaleheight is increased from ~ 490 pc at $t = 50$ Myr to ~ 950 pc, which is an increase of a factor of ~ 2 . Typically, the VFFs change significantly because the atomic hydrogen component is driven to large heights above the mid-plane as it

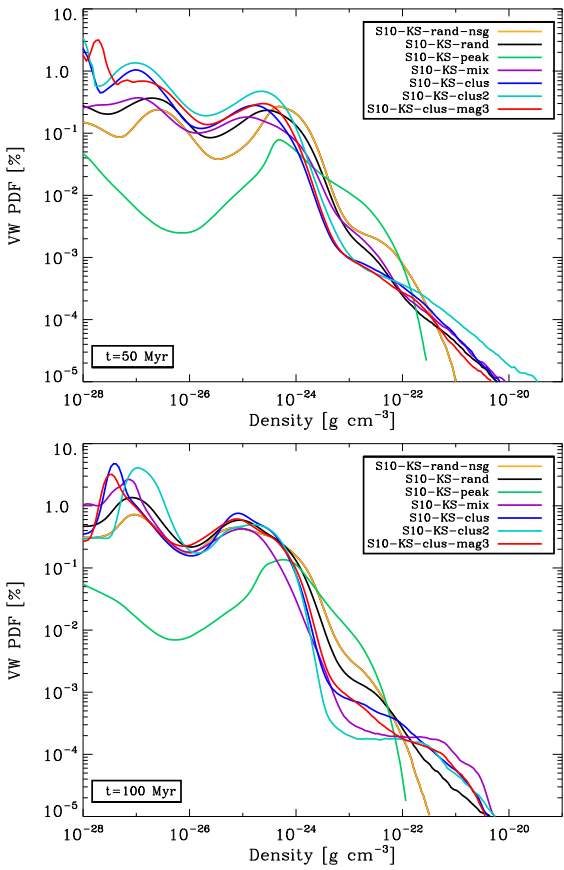


Figure 14. Volume-weighted density PDFs of runs *S10-KS-rand-nsg*, *S10-KS-rand*, *S10-KS-peak*, *S10-KS-mix*, *S10-KS-clus*, *S10-KS-clus2*, and *S10-KS-clus-mag3* at $t = 50$ Myr (top panel) and $t = 100$ Myr (bottom panel). The PDFs are very similar, in particular for the more evolved snapshot. The major difference is the lack of dense gas without self-gravity as well as in the case of peak driving.

traces the developing galactic outflow. The outflows have a complex multiphase structure and entrain significant amounts of ionized gas and warm atomic gas (see SILCC2).

7 THE PHASES OF THE ISM

In the following, we discuss the PDFs of the different chemical species or, respectively, gas temperature phases, in more detail. Previous studies of stratified discs (e.g. Joung & Mac Low 2006; Gent et al. 2013b; Kim & Ostriker 2015), have not employed a chemical network to distinguish between molecular and atomic or ionized gas, and have therefore used temperature cuts to estimate the amount of molecular hydrogen that forms in the simulations. Here, we show that the chemical composition is complicated and cannot be easily separated into distinct temperature/density phases. We note that, traditionally, the temperature phases of the ISM are defined as follows (e.g. Mihalas & Binney 1981):

- (i) Molecular ($T \leq 30$ K): very cold and dense gas, which is most likely in molecular form.
- (ii) Cold ($T < 300$ K): thermally stable cold gas.
- (iii) Warm ($300 \text{ K} \leq T < 10^4$ K): warm atomic and ionized gas.
- (iv) Warm-hot ($10^4 \text{ K} \leq T < 3 \times 10^5$ K): highly ionized gas in the thermally unstable regime.
- (v) Hot ($T \geq 3 \times 10^5$ K): very hot gas, mostly in hot SN remnants.

7.1 Chemical composition versus temperature/density phases

In Fig. 20, we plot the mass-weighted and volume-weighted density PDFs of run *S10-KS-clus-mag3*. The PDFs are split up into individual contributions according to the actual chemical composition (left-hand panels), or gas temperature phase (right-hand panels), respectively. The mass-weighted density PDF appears different when split up by temperature phase rather than chemical composition. The distributions of H^+ and H are very broad and overlap significantly, in particular in the thermally unstable regime. We note

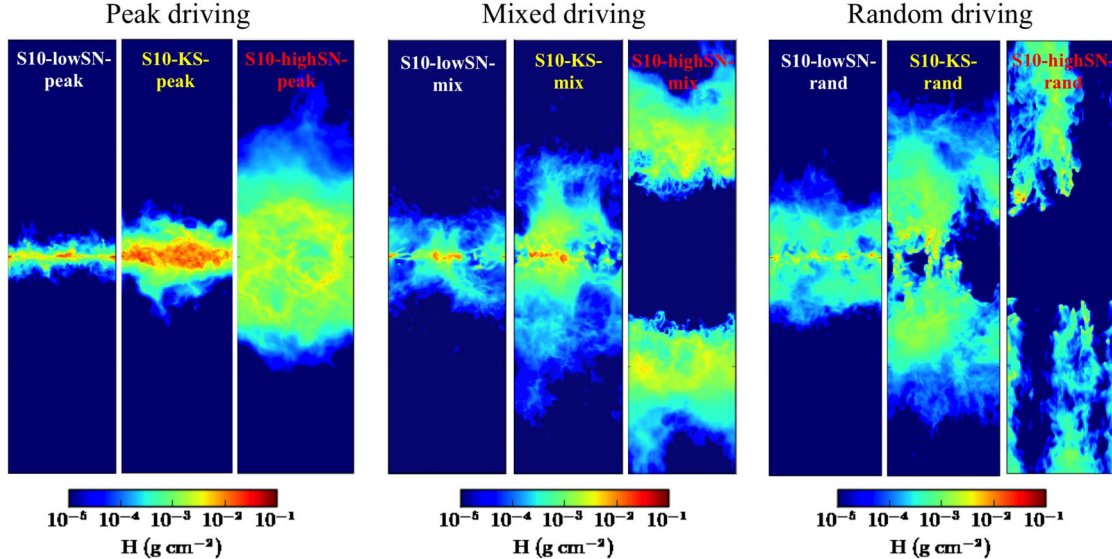


Figure 15. Projections showing the atomic hydrogen distribution for runs with different SN rates and different driving modes at $t = 50$ Myr. From left to right: peak driving runs with low SN rate (*S10-lowSN-peak*), KS SN rate, and high SN rate (*S10-highSN-peak*); mixed driving runs with low SN rate (*S10-lowSN-mix*), KS SN rate, and high SN rate (*S10-highSN-mix*); and random driving runs with low SN rate (*S10-lowSN-rand*), KS SN rate, and high SN rate (*S10-highSN-rand*). For all driving modes, the SN rate determines the vertical scaleheight of the gas. The discs are thin for low SN rates and completely blown apart for mixed and random driving at a high SN rate (peak driving is puffed up in this case).

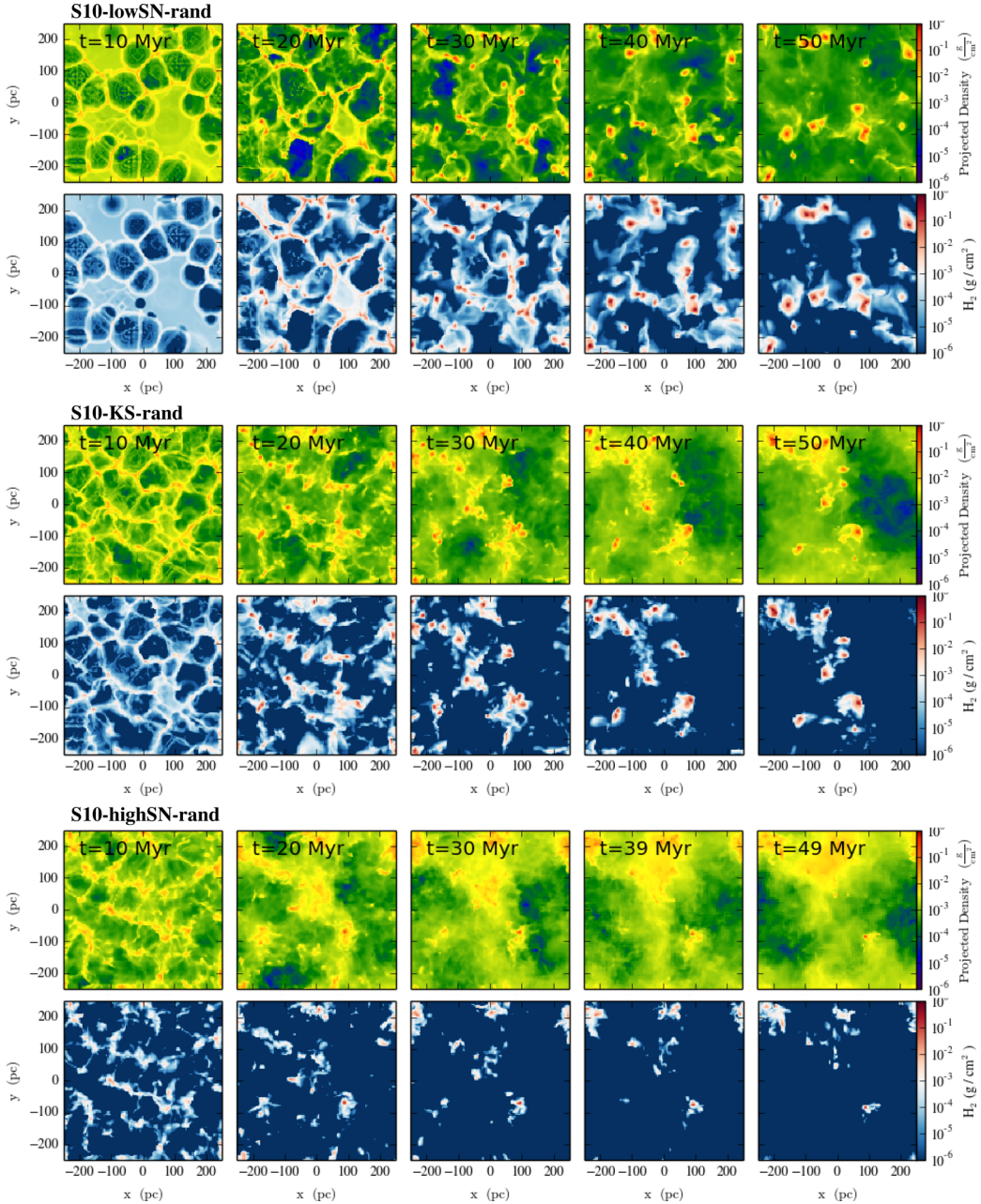


Figure 16. Time evolution of total and H_2 column densities (as in Fig. 13) for runs with different SN rates, i.e. $S10\text{-lowSN-rand}$ (top), $S10\text{-KS-rand}$ (middle), and $S10\text{-highSN-rand}$ (bottom). The SN rate strongly influences the morphology of the gas as well as the total amount of formed molecular gas (see Fig. 17). With increasing SN rate the structure of the ISM becomes more diffuse.

that the H^+ contribution might be underestimated at high densities due to the absence of ionizing radiation from massive stars. At high densities (above $n \sim 100 \text{ cm}^{-3}$), there is still some atomic hydrogen, which represents the thermally stable, cold neutral medium (CNM), but the medium is predominantly molecular. The dashed purple line shows the amount of molecular gas predicted from using simple density and temperature cuts ($T \leq 30 \text{ K}$ and $n \geq 100 \text{ cm}^{-3}$). It is inconsistent with the actual mass and distribution of molecular gas (H_2 and CO) since most of the H_2 at densities $n \lesssim 10^4 \text{ cm}^{-3}$ is warm. Therefore, the total mass in molecular gas would be underpredicted by a factor of 3 in this run at $t \approx 50 \text{ Myr}$ when using this simple density and temperature cut-off. Overall, we might still underestimate the H_2 fraction in lower density gas due to our limited resolution,

with which we cannot resolve small-scale clumping, which enables and accelerates the formation of molecular hydrogen in this regime (Glover & Mac Low 2007a).

The volume-weighted density PDFs are in better agreement, at least for the hot and warm gas and H^+ and H , respectively. The thermally stable, cold gas again consists of a combination of atomic hydrogen (mostly CNM) and molecular medium. Again, the simple density–temperature cut estimates a much smaller amount and distribution of molecular hydrogen than the distribution extracted from the simulation, which dynamically follows the formation and dissociation of H_2 and CO. More of the H_2 could possibly be captured in post-processing if a modified density cut-off most is used, e.g. $n \sim 50 \text{ cm}^{-3}$ and $T < 100 \text{ K}$, but it is impossible to determine

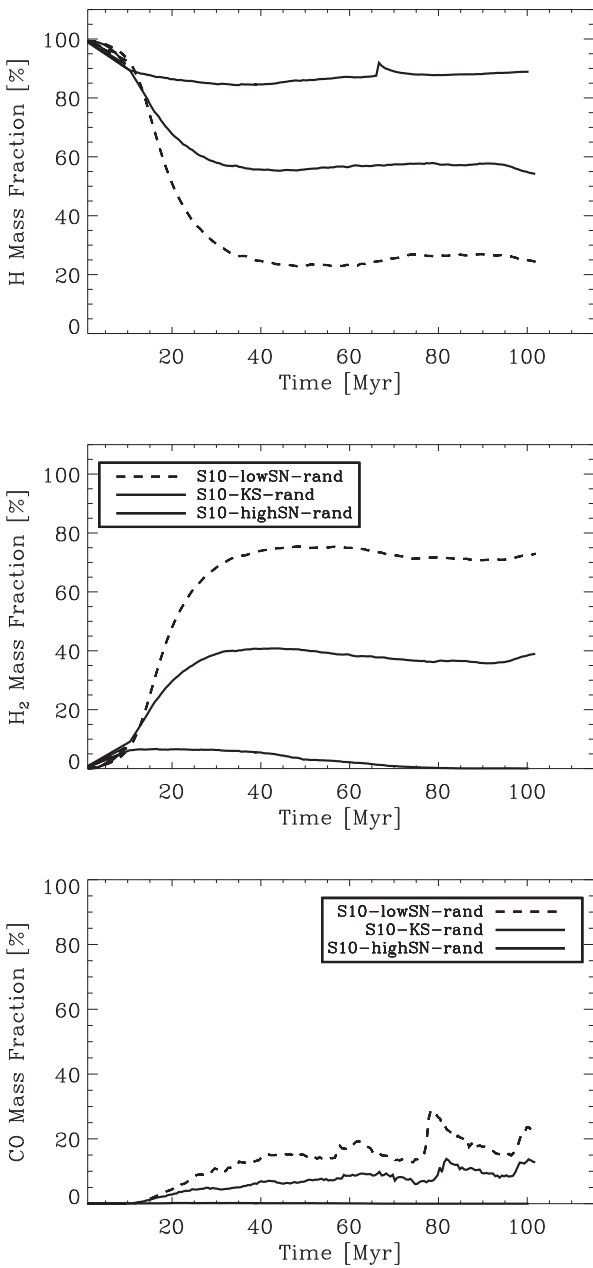


Figure 17. H (top) and H₂ (middle) mass fractions (with respect to the total hydrogen mass) and CO mass fraction (bottom; with respect to the total mass in carbon) as a function of time for runs with random driving using three different SN rates to estimate the influence of the star formation feedback efficiency on the chemical composition of the gas. We show run *S10-lowSN-rand* where the SN rate is a factor of 3 times lower than the KS rate, i.e. five SNe per Myr (dashed line), run *S10-KS-rand* which uses the KS SN rate at 15 Myr⁻¹ (solid line), and *S10-highSN-rand* with an SN rate of 45 Myr⁻¹ (dash-dotted line). We find significantly less cold and molecular gas with increasing SN rates.

reliable cut-off values which are generally valid and constant in time.

In Fig. 21, we show the mass-weighted and volume-weighted temperature PDFs for the different chemical components. The grey dashed lines indicate the temperature thresholds used in the simple phase classification. All the chemical components are spread out over two or more temperature regimes, which explains the major differences we see in the density PDFs.

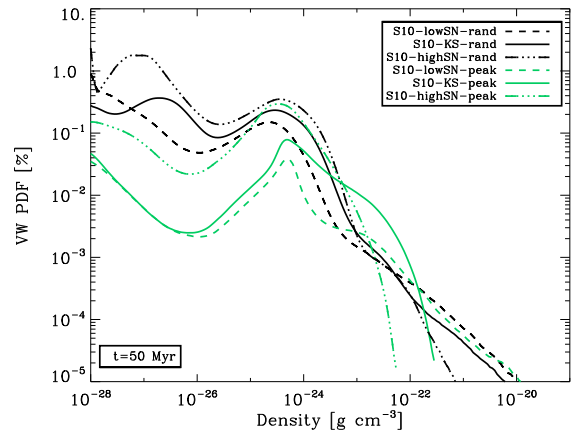


Figure 18. Volume-weighted density PDFs of runs with different SN rates for random driving (black lines), i.e. *S10-lowSN-rand*, *S10-KS-rand*, and *S10-highSN-rand*, and peak driving (green lines), i.e. *S10-lowSN-peak*, *S10-KS-peak*, and *S10-highSN-peak*. With increasing SN rate the PDF becomes narrower since the distribution is truncated at high densities, which essentially leaves two phases (warm at around $\rho \approx 10^{-24}$ g cm⁻³ and hot at $\rho \approx 10^{-27.5}$ g cm⁻³).

In general, none of the total PDFs has a simple lognormal shape or consists of a combination of lognormal distributions as e.g. found in Hennebelle & Ifrig (2014), who use a simpler cooling description. Concerning the individual components, only the volume-weighted distribution of H₂ is consistent with a broad lognormal shape plus a high-density power-law tail, which is expected to develop due to local gravitational collapse (Klessen, Heitsch & Mac Low 2000; Slyz et al. 2005; Kainulainen et al. 2009; Schneider et al. 2011; Girichidis et al. 2014a). We note that, since the real ISM is neither isothermal nor stirred via coherent large-scale forcing, deriving a turbulent Mach number from fitting a lognormal function to an observed density PDF can easily lead to unreliable results and should be used with caution. For instance, the cold phase in the volume-weighted PDF in Fig. 20 (lower-right panel) looks like a lognormal + power-law tail, but the lognormal part towards lower densities can be arbitrarily shifted by choosing a different temperature cut off to define the cold phase and should therefore not be used for fitting.

7.2 Phase diagrams

In the traditional view, the different phases of the ISM, in particular the warm and the cold phase, can co-exist in approximate pressure equilibrium (Field 1965; McKee & Ostriker 1977). This picture has been revised since models of turbulent flows under the influence of heating and cooling have shown that the phase space (temperature-density or pressure-density) distributions of the gas are broad due to turbulent heating in dissipative shocks on the one hand, and cooling by expansion on the other hand (Vazquez-Semadeni 2009; Seifried, Schmidt & Niemeyer 2011; Walch et al. 2011; Micic et al. 2013; Saury et al. 2014).

In Fig. 22, we plot the temperature-density (left-hand column) and pressure-density (right-hand column) distributions of runs *S10-KS-rand-nsg* (top row), *S10-KS-rand* (second row), *S10-KS-peak* (third row), and *S10-KS-clus-mag* (bottom row) at $t = 50$ Myr using 150 bins in log density and log temperature. We overplot the mean pressure for each density bin, P_{mean} (solid black line), as well as the average pressure of the different phases $\langle P_{\text{mean}} \rangle$ (blue

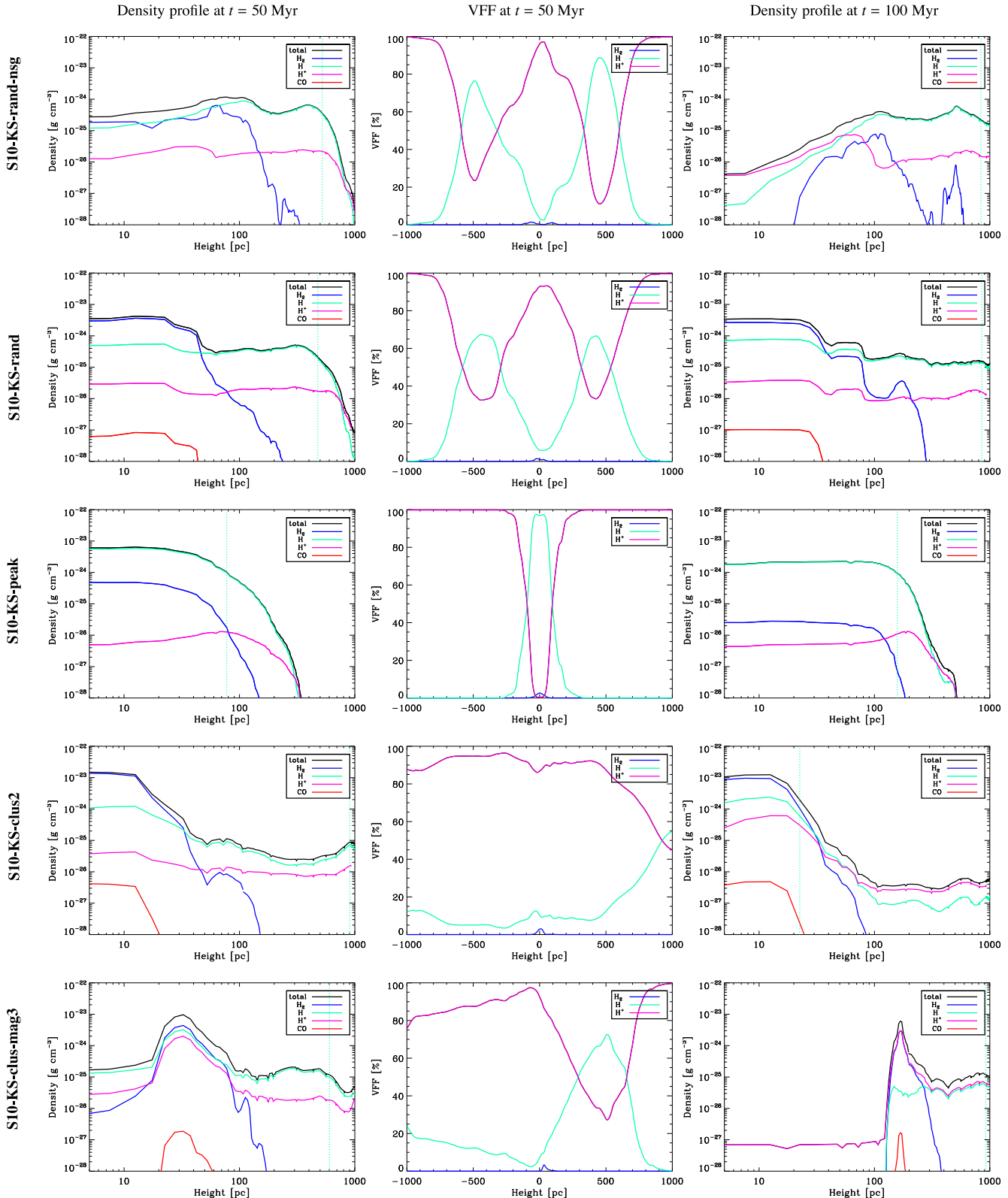


Figure 19. Left-hand column: mean vertical density profiles of the total density, H^+ , H , H_2 , and CO taken at $t = 50 \pm 2.0$ Myr. We also average over positive and negative z -direction. The dotted green line indicates the vertical height, which encloses 90 per cent of the atomic hydrogen mass (see also Table 2). Middle column: vertical profiles of the corresponding VFFs of at $t = 50 \pm 2.0$ Myr. Usually, the VFF of the molecular gas is negligible and H and H^+ provide the main contributions. Right-hand column: density profiles at $t = 100 \pm 2$ Myr. The disc appears to be significantly more extended than at $t = 50$ Myr as a significant amount of mass (primarily in $H I$) is entrained in an outflow. From top to bottom we compare runs *S10-KS-rand-nsg*, *S10-KS-rand*, *S10-KS-peak*, *S10-KS-clus2*, and *S10-KS-clus-mag3*. For clustered driving, the discs become asymmetric causing an offset in the peak density with respect to the mid-plane at $z = 0$.

Table 2. Vertical height which encloses 90 per cent of the atomic hydrogen mass at $t \sim 50$ Myr. From top to bottom, we list runs with random driving but without self-gravity, with random driving and self-gravity, with peak driving, mixed driving, clustered Type II SNe, and with partly clustered, partly random Type II SN driving plus the more extended Type Ia component, with and without magnetic fields.

SN implementation	Low SN	KS	High SN
Ng-rand	–	510 pc	–
Rand	192 pc	490 pc	932 pc
Peak	43 pc	77 pc	368 pc
Mix	133 pc	298 pc	668 pc
Clus2	–	902 pc	–
Clus	–	588 pc	–
Clus-mag3	–	602 pc	–

dashed horizontal line). For comparison, we also show the mid-plane pressure as estimated by Blitz & Rosolowsky (2006):

$$P_{\text{BR06}}/k_B = \Sigma_{\text{GAS}} v \sqrt{2 G \rho_\star}/k_B = 9965 [\text{K cm}^{-3}], \quad (35)$$

where v is the vertical velocity dispersion of the gas, which we set to $v = 8 \text{ km s}^{-1}$, following Koyama & Ostriker (2009, green dashed horizontal line). In addition, we overplot the equilibrium curve (blue dotted line) computed using the chemical network with a constant external hydrogen column density of $N_{\text{H,tot}} = 3 \times 10^{18} \text{ cm}^{-2}$ (see equation 18) and without considering the self-shielding of H_2 and

CO. We see that P_{BR06} touches the equilibrium curve at its local maximum at a density of a few $\times 10^{-24} \text{ g cm}^{-3}$.

The warm unstable gas traces the equilibrium curve, but at high densities the gas is colder than predicted since our adoption of a fixed value of $N_{\text{H,tot}}$ for computing the equilibrium curve dramatically underestimates the actual amount of dust shielding in the high-density gas. At a given density, we find a range of temperatures for three reasons. First, turbulence broadens the phase space distribution as kinetic energy is thermalized quickly and may heat gas to temperatures above the equilibrium curve. Secondly, the optical depth is not constant throughout the volume and thus, cells which are highly shielded are cooled to temperatures below the equilibrium curve, whereas cells which sit at lower optical depths have higher temperatures than the ones estimated with $N_{\text{H,tot}} = 3 \times 10^{18} \text{ cm}^{-2}$. A factor of 10 in $N_{\text{H,tot}}$ can easily change the temperature by a factor of 5 in the thermally unstable regime. Thirdly, cooling by expansion causes low density, cool gas below the equilibrium curve.

All four simulations have two distinct phases (warm and cold) in approximate pressure equilibrium with each other. Also, the pressure of the low density, hot phase, which consists of SN shock heated gas, seems to be roughly in pressure equilibrium with the warm phase. However, the pressure distribution at low densities is very broad and spans about five orders of magnitude where SN shock heated and adiabatically cooled gas is both present. Only run S10-KS-peak with peak driving does not show the otherwise

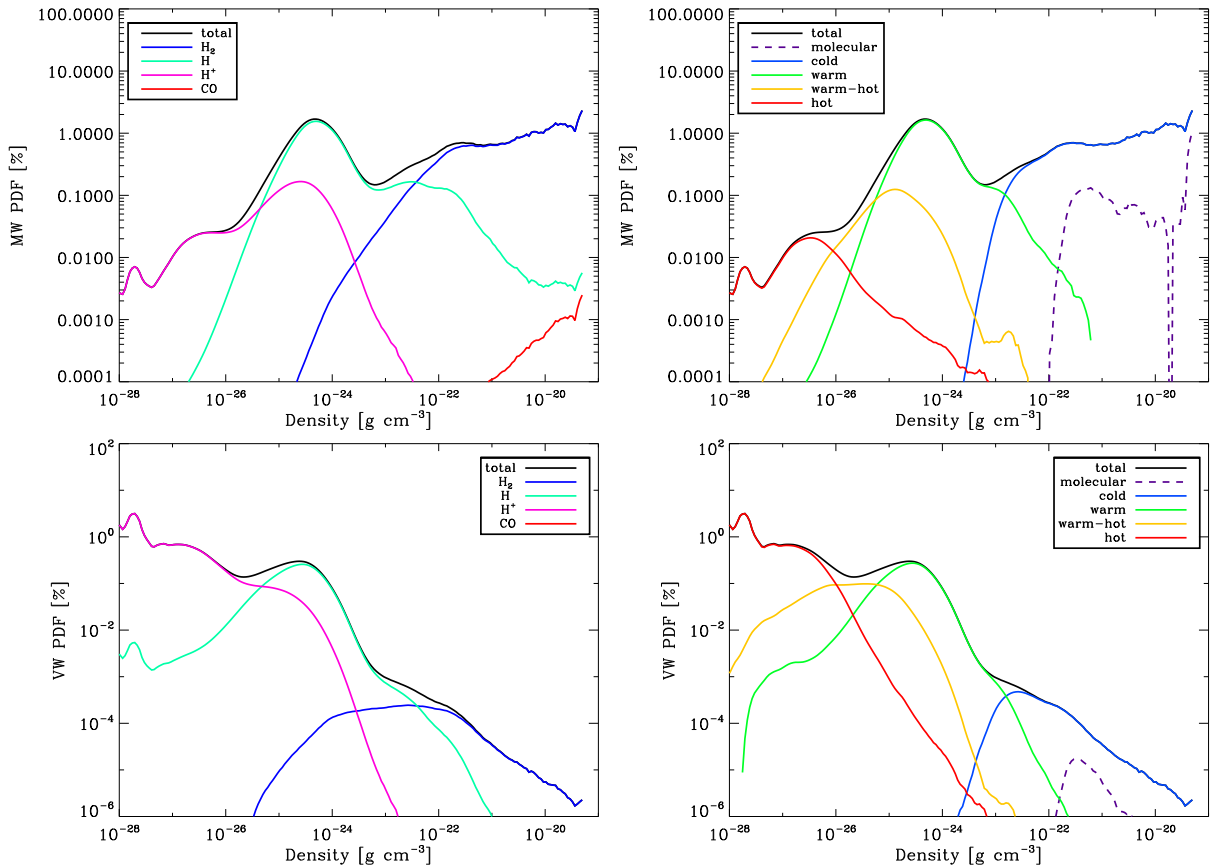


Figure 20. Mass-weighted (first row) and volume-weighted (second row) density PDFs around $t = 50 \pm 2.0$ Myr for run S10-KS-clus-mag3. We take the mean of 10 simulation snapshots, which are separated by 0.5 Myr. The left-hand column shows the contributions according to the chemical composition and the right-hand column shows the contributions according to the temperature distribution of the gas. We find that the composition derived from the temperature classification generally does not reflect the gas chemistry.

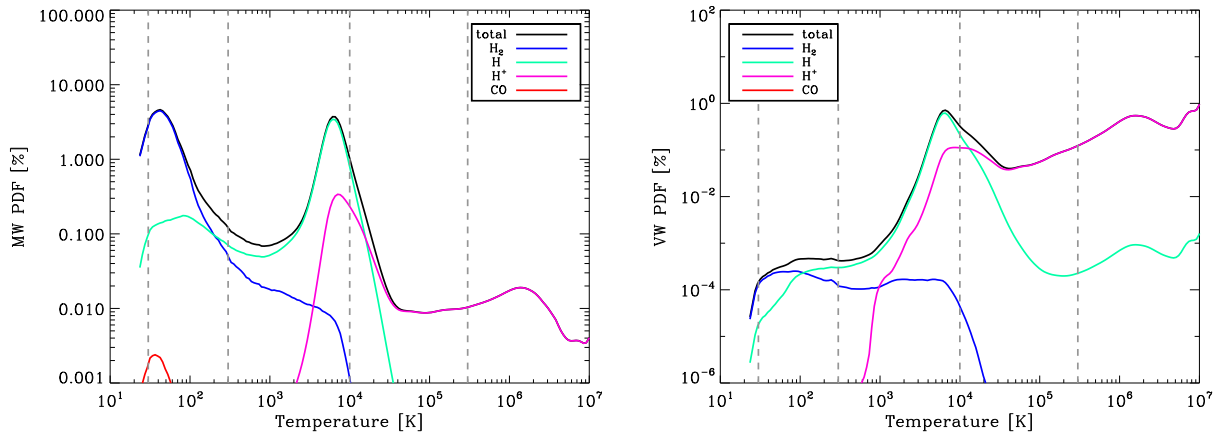


Figure 21. Mass-weighted (left) and volume-weighted (right) temperature PDFs at $t = 50 \pm 2.0$ Myr for run *S10-KS-clus-mag3*. The grey dashed lines indicate the five different temperature regimes we consider in the temperature classification. Each chemical component is spread out over two or more temperature regimes.

obvious warm and cold phases, since there is too much gas in the thermally unstable regime. The hot phase is completely absent in this case and pressure equilibrium is not established at all. In addition, the peak driving run shows the largest offset between the mean gas pressure (P_{mean}) and P_{BR06} .

Also for the run without self-gravity, there is a larger difference between $\langle P_{\text{mean}} \rangle$ and P_{BR06} than for runs *S10-KS-rand* and *S10-KS-clus-mag*, where run *S10-KS-clus-mag* is closer to P_{BR06} . This is caused by the absence of the cold branch at high densities, which increases $\langle P_{\text{mean}} \rangle$ further towards P_{BR06} for the latter two simulations. There, the cold gas stretches towards high pressures ($P_{\text{mean}}/k_B \approx 10^5\text{--}10^6 \text{ K cm}^{-3}$), thereby following a roughly isothermal behaviour with $T \sim 30$ K. The fact that all gas with $\rho \gtrsim 10^{-21} \text{ g cm}^{-3}$ is overpressured with respect to the warm and hot phases in addition to the fact that gas at higher densities is absent without self-gravity, indicates that self-gravity dominates above this density threshold. The general estimate that the hot gas pressure adjusts to the local pressure that is expected for a given galaxy (Ostriker, McKee & Leroy 2010) is met very well in our simulations. A more thorough investigation of all pressure components (thermal, kinetic, and magnetic) is given in the companion paper (SILCC2).

8 CHEMICAL COMPOSITION AND VFFS

Recently, high-resolution data has greatly enhanced our understanding of the gaseous ISM in different galaxies. In the previous section, we have shown that the mean thermal pressures derived for our models with random or clustered driving are in good agreement with observed estimates. Here, we will shortly summarize the findings on the mass fractions of H, H₂, and CO, and on the VFFs of the different gas phases.

8.1 Mass fractions

To give a final overview of the mean H, H₂, and CO mass fractions that develop in our simulations, we plot the average values between 30 and 50 Myr (filled symbols), as well as the average between 30 Myr and the end of the respective simulation (open symbols) in Fig. 23. We find that the run without self-gravity leads to very low H₂ fractions of the order of ∼5 per cent. With self-gravity and with

an increasing SN rate, the H₂ mass fraction clearly decreases (see random (black symbols), peak (green symbols), and mixed driving (purple symbols)). In addition, peak driving hinders the formation of H₂ as long as the dense gas can be dispersed by SN explosions. Therefore, the H₂ mass fraction is below 5 per cent for runs *S10-highSN-peak* and *S10-KS-peak*, but quite high with ∼70 per cent for *S10-lowSN-peak*, where the SN energy input is not efficient enough to dissociate the H₂.

For random driving at a low SN rate (*S10-lowSN-rand*), we find H₂ mass fractions of ∼70 per cent, for the KS rate (*S10-KS-rand*) we find ∼40 per cent, and for the highest SN rate there is less than 5 per cent H₂. Similar, although slightly higher, values are obtained for the case of mixed driving, which mimics an extreme case of clustered driving (only one major colliding flow), and therefore gives similar H₂ fractions as the clustered driving runs. All clustered driving runs are very similar, regardless of whether a more extended Type Ia component is included or not. Magnetic fields slightly delay the H₂ formation, and therefore the time average is slightly below the values obtained without magnetic fields.

The mass fractions of atomic hydrogen are inversely proportional to the H₂ mass fractions, minus a small contribution from ionized hydrogen of ∼5–10 per cent. Moreover, the trends in the CO mass fractions are proportional to the H₂ mass fractions.

In the Milky Way, the molecular gas mass fraction drops from ∼50 per cent at a Galactocentric radius of 6.5 kpc to ∼2 per cent at a distance of 9.5 kpc (Honma, Sofue & Ariimoto 1995). The so-called ‘molecular front’ is caused by a roughly exponential decrease of the molecular gas mass with Galactocentric radius, while the atomic mass is distributed approximately evenly. Schruba et al. (2011) use the IRAM HERACLES survey (Leroy et al. 2009) to determine the molecular to atomic gas mass fractions as a function of radius for 33 spiral galaxies. For disc annuli with the given total gas surface density of $10 \text{ M}_\odot \text{ pc}^{-2}$, they find that the H₂-to-H surface density ratio varies between 0.1 and ∼15, with most of the galaxies having ratios between 0.1 and 1. The large variation at this particular total gas surface density arises as a result of a transition from a molecular dominated regime to gas, which consists mostly of atomic hydrogen (see also the theoretical work of Krumholz & Matzner 2009). Therefore, we may say that our findings are consistent with the observations, although the scatter is so large that even the run without self-gravity can provide a reasonable

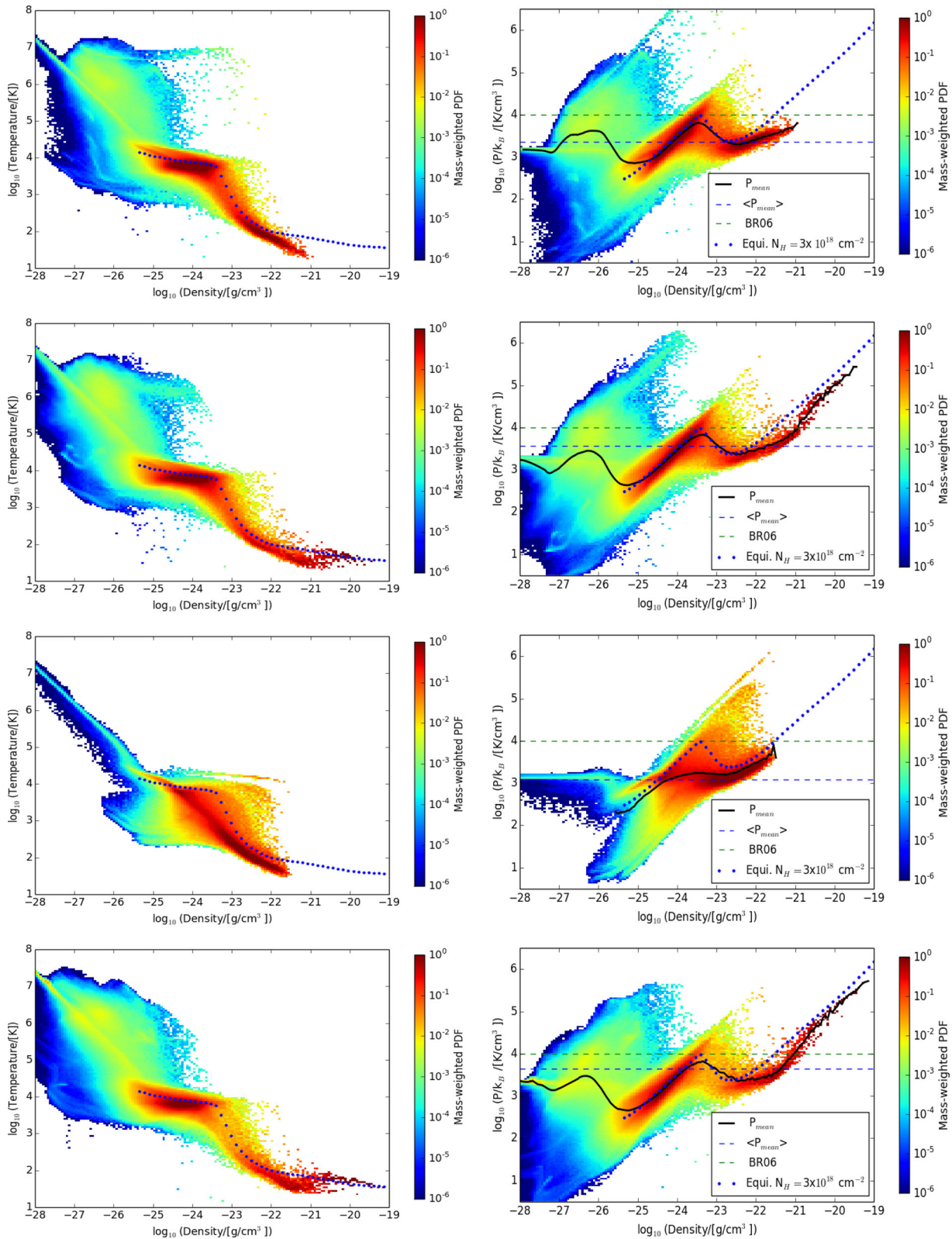


Figure 22. Mass-weighted phase space probability distributions for runs *S10-KS-rand-nsg* (top row), *S10-KS-rand* (second row), *S10-KS-peak* (third row), and *S10-KS-clus-mag3* (bottom row) at $t = 50$ Myr. We over plot the mean pressure for every density bin, P_{mean} (black lines), the average pressure computed as $\langle P_{\text{mean}} \rangle$ (blue dashed lines), and the mid-plane pressure derived from Blitz & Rosolowsky (2006), $P_{\text{BR06}}/k_B = 9965 [\text{K cm}^{-3}]$ (see equation 35; green dashed lines), as well as the equilibrium curve (blue dotted line), which was computed with a constant hydrogen column density of $N_{H,\text{tot}} = 3 \times 10^{18} \text{ cm}^{-2}$ (see equation 18) and without considering self-shielding of H₂ and CO.

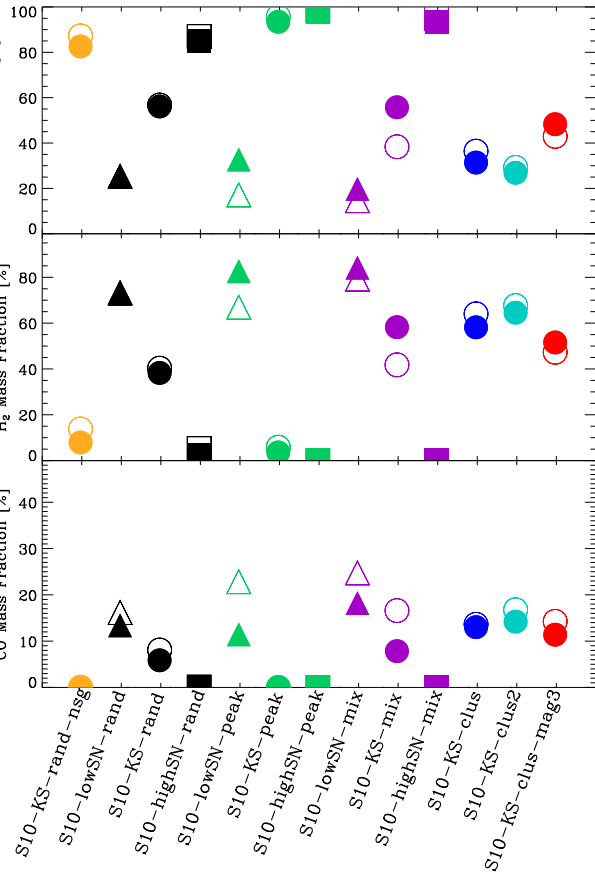


Figure 23. Time-averaged mass fractions of atomic hydrogen (top), H_2 (middle), and CO (bottom) for all simulations presented in this paper. H and H_2 mass fractions are computed with respect to the total hydrogen mass and CO is computed with respect to the total mass in carbon. Filled symbols show the average values within 30–50 Myr, and open symbols show the averages from 30 Myr onwards until the end of the simulation. Without self-gravity, the molecular gas fraction is significantly reduced. The SN rate as well as the SN positioning with respect to the dense gas are important drivers of the molecular phase. The highest H_2 fractions are obtained for clustered driving and for mixed driving at low SN rates (5 Myr^{-1}). The presence of a magnetic field delays the formation of H_2 .

fit ($M_{H_2}/M_H \sim 0.065$ in this case). We will further investigate how the mass ratios translate into surface density ratios.

8.2 Volume filling fractions

An analysis of the VFFs for different temperature phases is often used to establish an overview of the structure of the multiphase ISM and attempt to disentangle what drives its evolution. We show the VFFs for all runs in five different temperature regimes (see Section 7) within $z = \pm 2 \text{ kpc}$ around the disc mid-plane in Fig. 24 and within $z = \pm 150 \text{ pc}$ in Fig. 25. Like for the total mass fractions, we average the VFFs from 30 Myr onwards until the end of the simulations.

In Fig. 24, we find that the VFFs are always dominated by hot gas, whereas the warm and cold phases contribute less than 20–30 per cent and less than 0.1 per cent, respectively. Also, the VFFs are very robust if the SNe preferentially explode in low-density environments. In these cases, neither the absence of self-gravity, nor

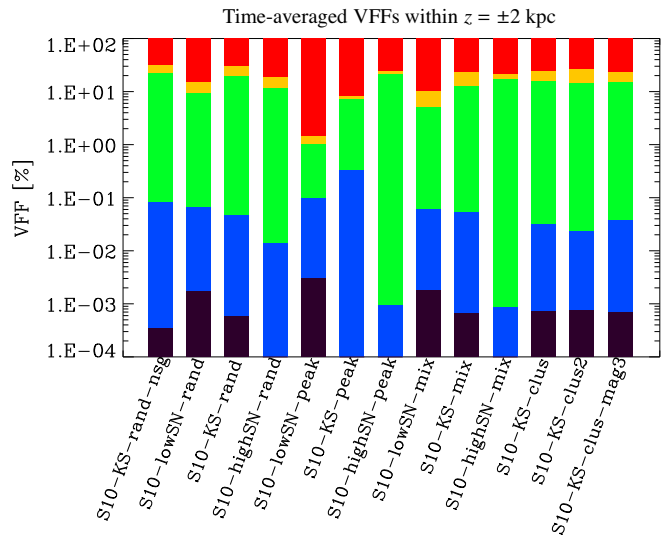


Figure 24. Time-averaged VFFs of ISM phases in different temperature regimes for all simulations. We only count gas within $\pm 2 \text{ kpc}$ in the vertical direction. To minimize the effect of fluctuations, we average from 30 Myr onwards until the end of each simulation. The colour-coding is the following: purple: cold, molecular gas with $T < 30 \text{ K}$; blue: cold, atomic gas with $T < 300 \text{ K}$; green: warm gas with $300 \text{ K} \leq T < 12\,000 \text{ K}$; yellow: warm, ionized medium with $12\,000 \text{ K} \leq T < 300\,000 \text{ K}$; red: hot, ionized medium with $T \geq 300\,000 \text{ K}$.

clustering or magnetic fields change the mean VFFs significantly. There is a clear trend that a higher SN rate fills the volume with less molecular gas but more cold and warm gas, while, interestingly, the hot gas VFF is rather reduced with increasing SN rate. The reason for the latter is the onset of a larger scale outflow, which fills a significant volume within the inner 2 kpc around the disc mid-plane. Only in the case of random driving this is not applicable anymore, since the run with a high SN rate completely disrupts the disc and leads to a hotter ISM. Overall, a clear difference in the VFF distributions can only be seen for random, peak, and mixed driving at different SN rates.

From Fig. 25, we find that even close to the disc mid-plane the volume is mostly filled with hot gas (up to 80 per cent for our fiducial runs!). In addition, a significant fraction (10–20 per cent) is filled with warm-hot gas in the thermally unstable regime, while the warm gas only contributes ~ 5 –10 per cent. It seems that our models are in agreement with the classical three-phase ISM model (McKee & Ostriker 1977), where hot gas fills the intercloud volume. This is in contradiction to simulations by de Avillez & Breitschwerdt (2004), Joung & Mac Low (2006) and Hill et al. (2012), who find that most of the volume is filled with a pervasive, warm medium (VFF ~ 50 per cent) while the VFF of the hot gas component is smaller and where the hot gas is mostly found in embedded SN bubbles.

For different SN positioning and SN rates, we find the following trends. For random and mixed driving, a higher SN rate increases the hot gas VFF. For peak driving, the opposite behaviour is found with a vanishing hot gas VFF for the run with the highest SN rate (45 Myr^{-1} , run *S10-highSN-peak*), while run *S10-lowSN-peak* appears to have a hot gas VFF of 80 per cent. Therefore, a high hot gas VFF can also be caused by a vertically concentrated disc morphology.

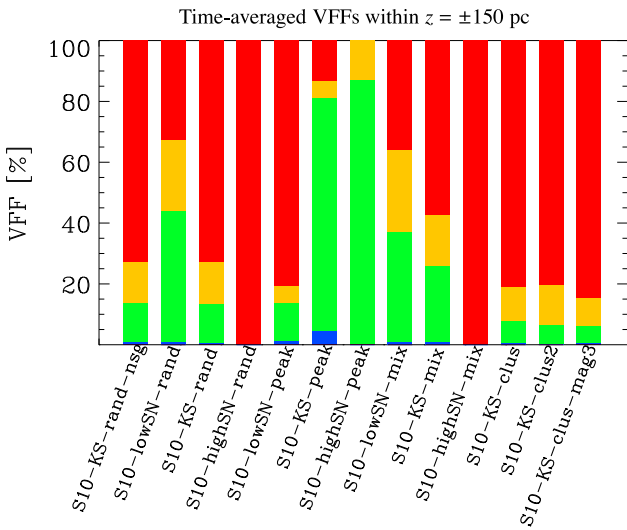


Figure 25. Time-averaged VFFs of different temperature regimes, similar to Fig. 24, for gas within ± 150 pc. Even close to the disc mid-plane most of the volume (~ 80 per cent for our fiducial runs) is filled with hot gas (red), and a non-negligible fraction is filled with warm-hot gas (yellow) in the thermally unstable regime (10–20 per cent). Warm gas (green) makes up for another ~ 5 –10 per cent, and cold, atomic gas (blue) contributes $\lesssim 1$ per cent in most cases.

9 CONCLUSIONS

We present a self-consistent study of molecular gas formation in a stratified galactic disc, which develops a turbulent, multiphase ISM under the influence of self-gravity, SN explosions, and (in one simulation) magnetic fields. We choose conditions resembling the Milky Way disc near the solar neighbourhood. The fully three-dimensional simulations have been carried out with the MHD code FLASH 4, which has been significantly extended to include the necessary additional physics.

We find that self-gravity is most important in dense gas. Without self-gravity, it is impossible to obtain reliable estimates of the amount of dense, molecular gas in the simulations. In addition, models without self-gravity converge to an arbitrary ISM structure with roughly constant mass fractions within the different chemical components, which can easily be misinterpreted as the establishment of a dynamical equilibrium in these models (after $t \sim 50$ Myr). With self-gravity, the simulations do not evolve towards a dynamical equilibrium state since dense molecular clouds form and merge, but are generally not destroyed again. This long-term evolution of the dense molecular clouds would be changed if star formation and stellar feedback, in particular ionizing radiation and stellar winds, would be included self-consistently.

Globally, the external gravitational potential dominates the initial evolution of the gas as it initiates a collapse towards the mid-plane. Furthermore, the interplay of the external potential and the turbulent and thermal pressure provided by the SN feedback sets the vertical distribution of the warm neutral medium seen in atomic hydrogen.

We explore the impact of different descriptions used for SN driving by changing the positions relative to the dense clouds or the rate of explosions in different simulations. We investigate five distinct cases: (1) random SN driving; (2) peak SN driving, where the explosion is always placed at the global density maximum; (3) mixed SN driving with a fraction of 50 per cent peak and 50 per cent random driving; (4) clustered Type II SN driving; and (5) clustered driving

that also includes a population of Type Ia's (20 per cent), which have a broader vertical distribution. Moreover, we vary the SN rate. As a fiducial value we take the typical value derived from the KS relation at $\Sigma_{\text{GAS}} = 10 \text{ M}_\odot \text{ pc}^{-2}$, which results in an SN rate of 15 Myr^{-1} in the simulated volume. Since this value is quite uncertain, we scale it up by a factor of 3 (to 45 Myr^{-1}) and down by a factor of 3 (to 5 Myr^{-1}).

We find that both the SN rate and position have a major impact on the amount of molecular gas formed as well as on the vertical distributions of the gas. For the low and KS SN rates and random, mixed, or clustered driving we do recover a disc structure which is in good agreement with the Milky Way. However, for high SN rates the discs are mostly dispersed, which implies that self-consistent star formation at such a high level could not be maintained. For peak driving many properties of the resulting ISM are not in agreement with observations (e.g. VFFs, mass fractions). Compared to the impact of the different SN rates, and peak or mixed versus random driving, the additional clustering of SNe has a minor effect on the mass distributions, the VFFs, and the phases of the ISM in general.

Also magnetic fields change the amount of dense and cold gas formed. With moderate initial magnetic fields ($3 \mu\text{G}$), we find that the additional magnetic pressure is significant in dense gas and thus delays the formation of dense and cold, molecular gas. Magnetic fields therefore seem to be important for determining the onset and time-scale of molecular cloud formation. However, they do not change the overall evolution of the disc on longer time-scales. We will explore their impact in more detail in a subsequent paper. In any case, magnetic fields and self-gravity have to be included at the same time as the amount of cold and dense gas will be crucially underestimated in MHD runs without self-gravity.

Close to the disc mid-plane (within $z = \pm 150$ pc), the hot gas VFF is ~ 80 per cent for most runs, which is consistent with the three-phase model of McKee & Ostriker (1977). The hot gas pressure is in approximate equilibrium with the warm phase and, to within a factor of 2, the pressures are consistent with the estimates of Blitz & Rosolowsky (2006).

Our results indicate that the ISM structure is only in agreement with observations if a significant fraction of all SNe explodes in low-density environments. Runaway OB stars contribute to this ‘random’ SN component (Kimm & Cen 2014). In addition, early stellar feedback in the form of stellar winds and ionizing radiation can disperse molecular clouds before the first SNe explode. This lowers the environmental densities of Type II SNe. In star clusters, the first SN will also remove a significant fraction of the gas, which leads to beneficial conditions for subsequent explosions. The details of different feedback mechanisms within molecular clouds with different masses need to be further studied in future simulations.

ACKNOWLEDGEMENTS

The SILCC team thanks the anonymous referee for his/her useful comments, which helped to improve the paper. We further thank the Gauss Center for Supercomputing (<http://www.gauss-centre.eu/>) and the Leibniz-Rechenzentrum Garching (<http://www.lrz.de>) for the significant amount of computer time for this project and their user support as well as the Max Planck Computing & Data Facility for their support. Furthermore, we thank the Deutsche Forschungsgemeinschaft (DFG) for funding through the SPP 1573 ‘The physics of the interstellar medium’. SKW acknowledges the support of the Bonn-Cologne Graduate School for physics and astronomy as well as the SFB 956 on the ‘Conditions and impact of star formation’. RSK, SCOG, and CB thank the DFG for funding via the

SFB 881 ‘The Milky Way System’ (subprojects B1, B2, and B8). RSK furthermore acknowledges support from the European Research Council under the European Community’s Seventh Framework Programme (FP7/2007-2013) via the ERC Advanced Grant STARLIGHT (project number 339177). TN acknowledges support from the Cluster of Excellence ‘Origin and structure of the Universe’. RW acknowledges support by the Czech Science Foundation grant 209/12/1795 and by the project RVO:67985815 of the Academy of Sciences of the Czech Republic. TP acknowledges financial support through a Forschungskredit of the University of Zürich, grant no. FK-13-112. The software used in this work was developed in part by the DOE NNSA ASC- and DOE Office of Science ASCR-supported FLASH Center for Computational Science at the University of Chicago. To create some of the figures, we have used the free visualization software *yt* (yt-project.org Turk et al. 2011).

REFERENCES

- Agertz O., Lake G., Teyssier R., Moore B., Mayer L., Romeo A. B., 2009, MNRAS, 392, 294
- Agertz O., Kravtsov A. V., Leitner S. N., Gnedin N. Y., 2013, ApJ, 770, 25
- Aumer M., White S. D. M., Naab T., Scannapieco C., 2013, MNRAS, 434, 3142
- Bakes E. L. O., Tielens A. G. G. M., 1994, ApJ, 427, 822
- Banerjee R., Vázquez-Semadeni E., Hennebelle P., Klessen R. S., 2009, MNRAS, 398, 1082
- Barnes J., Hut P., 1986, Nature, 324, 446
- Bergin E. A., Hartmann L. W., Raymond J. C., Ballesteros-Paredes J., 2004, ApJ, 612, 921
- Bigiel F., Leroy A., Walter F., Brinks E., de Blok W. J. G., Madore B., Thornley M. D., 2008, AJ, 136, 2846
- Blitz L., Rosolowsky E., 2006, ApJ, 650, 933
- Blondin J. M., Wright E. B., Borkowski K. J., Reynolds S. P., 1998, ApJ, 500, 342
- Bohlin R. C., Savage B. D., Drake J. F., 1978, ApJ, 224, 132
- Bonnell I. A., Dobbs C. L., Smith R. J., 2013, MNRAS, 430, 1790
- Bouchut F., Klingenberg C., Waagan K., 2007, Numer. Math., 108, 7
- Bouchut F., Klingenberg C., Waagan K., 2010, Numer. Math., 115, 647
- Breitschwerdt D., 2008, Nature, 452, 826
- Brook C. B., Stinson G., Gibson B. K., Shen S., Macciò A. V., Obreja A., Wadsley J., Quinn T., 2014, MNRAS, 443, 3809
- Brown P. N., Byrne G. D., Hindmarsh A. C., 1989, SIAM J. Sci. Stat. Comput., 10, 1038ff
- Calzetti D. et al., 2007, ApJ, 666, 870
- Chabrier G., 2001, ApJ, 554, 1274
- Chabrier G., 2003, PASP, 115, 763
- Christensen C., Quinn T., Governato F., Stilp A., Shen S., Wadsley J., 2012, MNRAS, 425, 3058
- Clark P. C., Glover S. C. O., Klessen R. S., 2012, MNRAS, 420, 745
- Clarke C., Oey M. S., 2002, MNRAS, 337, 1299
- Creasey P., Theuns T., Bower R. G., 2013, MNRAS, 429, 1922
- Dale J. E., Bonnell I. A., Clarke C. J., Bate M. R., 2005, MNRAS, 358, 291
- Dale J. E., Ercolano B., Bonnell I. A., 2012, MNRAS, 424, 377
- Dalgarno A., McCray R. A., 1972, ARA&A, 10, 375
- de Avillez M., Breitschwerdt D., 2004, Ap&SS, 292, 207
- de Avillez M. A., Breitschwerdt D., 2005, A&A, 436, 585
- Dobbs C. L., Pringle J. E., 2013, MNRAS, 432, 653
- Dobbs C. L., Glover S. C. O., Clark P. C., Klessen R. S., 2008, MNRAS, 389, 1097
- Dobbs C. L., Burkert A., Pringle J. E., 2011, MNRAS, 417, 1318
- Dobbs C. L., Pringle J. E., Burkert A., 2012, MNRAS, 425, 2157
- Dorfi E. A., Breitschwerdt D., 2012, A&A, 540, A77
- Draine B. T., 1978, ApJS, 36, 595
- Draine B. T., Bertoldi F., 1996, ApJ, 468, 269
- Dubey A., Reid L. B., Weide K., Antypas K., Ganapathy M. K., Riley K., Sheeler D., Siegal A., 2009, preprint ([arXiv:0903.4875](https://arxiv.org/abs/0903.4875))
- Dubey A., Daley C., ZuHone J., Ricker P. M., Weide K., Graziani C., 2012, ApJS, 201, 27
- Ewald P. P., 1921, Ann. Phys., Lpz., 369, 253
- Field G. B., 1965, ApJ, 142, 531
- Fisher D. B., Bolatto A., Drory N., Combes F., Blitz L., Wong T., 2013, ApJ, 764, 174
- Förster Schreiber N. M. et al., 2011, ApJ, 739, 45
- Foster J. B., Mandel K. S., Pineda J. E., Covey K. R., Arce H. G., Goodman A. A., 2013, MNRAS, 428, 1606
- Fryxell B. et al., 2000, ApJS, 131, 273
- Gatto A. et al., 2015, MNRAS, 449, 1057
- Genel S. et al., 2014, MNRAS, 445, 175
- Gent F. A., Shukurov A., Sarson G. R., Fletcher A., Mantere M. J., 2013a, MNRAS, 430, L40
- Gent F. A., Shukurov A., Fletcher A., Sarson G. R., Mantere M. J., 2013b, MNRAS, 432, 1396
- Genzel R. et al., 2011, ApJ, 733, 101
- Girichidis P., Konstandin L., Whitworth A. P., Klessen R. S., 2014a, ApJ, 781, 91
- Girichidis P., Naab T., Walch S., Hanasz M., 2014b, preprint ([arXiv:1406.4861](https://arxiv.org/abs/1406.4861))
- Girichidis P. et al., 2015, MNRAS, preprint ([arXiv:1508.06646](https://arxiv.org/abs/1508.06646)) (SILCC2)
- Glover S. C. O., 2003, ApJ, 584, 331
- Glover S. C. O., Clark P. C., 2012a, MNRAS, 421, 9
- Glover S. C. O., Clark P. C., 2012b, MNRAS, 421, 116
- Glover S. C. O., Mac Low M., 2007a, ApJS, 169, 239
- Glover S. C. O., Mac Low M., 2007b, ApJ, 659, 1317
- Glover S. C. O., Federrath C., Mac Low M., Klessen R. S., 2010, MNRAS, 404, 2
- Gnat O., Ferland G. J., 2012, ApJS, 199, 20
- Gnedin N. Y., Tassis K., Kravtsov A. V., 2009, ApJ, 697, 55
- Goldsmith P. F., Langer W. D., 1978, ApJ, 222, 881
- Górski K. M., Hivon E., 2011, Astrophysics Source Code Library, record ascl:1107.018
- Habing H. J., 1968, Bull. Astron. Inst. Netherlands, 19, 421
- Hanasz M., Lesch H., Naab T., Gawryszczak A., Kowalik K., Wójtasiński D., 2013, ApJ, 777, L38
- Heitsch F., Stone J. M., Hartmann L. W., 2009, ApJ, 695, 248
- Heitsch F., Naab T., Walch S., 2011, MNRAS, 415, 271
- Hennebelle P., Ifrig O., 2014, A&A, 570, A81
- Hill A. S., Joung M. R., Mac Low M.-M., Benjamin R. A., Haffner L. M., Klingenberg C., Waagan K., 2012, ApJ, 750, 104
- Hirschmann M. et al., 2013, MNRAS, 436, 2929
- Hollenbach D., McKee C. F., 1989, ApJ, 342, 306
- Honma M., Sofue Y., Arimoto N., 1995, A&A, 304, 1
- Hopkins P. F., Quataert E., Murray N., 2011, MNRAS, 417, 950
- Hopkins P. F., Kereš D., Oñorbe J., Faucher-Giguère C.-A., Quataert E., Murray N., Bullock J. S., 2014, MNRAS, 445, 581
- Joung M. K. R., Mac Low M.-M., 2006, ApJ, 653, 1266
- Kafatos M., 1973, ApJ, 182, 433
- Kainulainen J., Beuther H., Henning T., Plume R., 2009, A&A, 508, L35
- Kennicutt R. C., Jr, 1998, ApJ, 498, 541
- Kevlahan N., Pudritz R. E., 2009, ApJ, 702, 39
- Kim C.-G., Ostriker E. C., 2015, ApJ, 802, 99
- Kim C.-G., Kim W.-T., Ostriker E. C., 2011, ApJ, 743, 25
- Kim C.-G., Ostriker E. C., Kim W.-T., 2013, ApJ, 776, 1
- Kimm T., Cen R., 2014, ApJ, 788, 121
- Klessen R., 1997, MNRAS, 292, 11
- Klessen R., Heitsch F., Mac Low M., 2000, ApJ, 535, 887
- Klingenberg C., Schmidt W., Waagan K., 2007, J. Comput. Phys., 227, 12
- Koyama H., Ostriker E. C., 2009, ApJ, 693, 1346
- Krumholz M. R., Matzner C. D., 2009, ApJ, 703, 1352
- Lee H.-H., Herbst E., Pineau des Forets G., Roueff E., Le Bourlot J., 1996, A&A, 311, 690
- Leitherer C. et al., 1999, ApJS, 123, 3
- Leroy A. K. et al., 2009, AJ, 137, 4670

- Li M., Ostriker J. P., Cen R., Bryan G. L., Naab T., 2015, preprint ([arXiv:1506.07180](https://arxiv.org/abs/1506.07180))
- McKee C. F., Ostriker J. P., 1977, ApJ, 218, 148
- Mac Low M.-M., McCray R., 1988, ApJ, 324, 776
- Marinacci F., Pakmor R., Springel V., 2014, MNRAS, 437, 1750
- Martizzi D., Faucher-Giguère C.-A., Quataert E., 2015, MNRAS, 450, 504
- Mathis J. S., Mezger P. G., Panagia N., 1983, A&A, 128, 212
- Matzner C. D., 2002, ApJ, 566, 302
- Micic M., Glover S. C. O., Federrath C., Klessen R. S., 2012, MNRAS, 421, 2531
- Micic M., Glover S. C. O., Banerjee R., Klessen R. S., 2013, MNRAS, 432, 626
- Mihalas D., Binney J., 1981, Galactic Astronomy: Structure and Kinematics, 2nd edn. Freeman & Co., San Francisco
- Murante G., Monaco P., Borgani S., Tornatore L., Dolag K., Goz D., 2015, MNRAS, 447, 178
- Nelson R. P., Langer W. D., 1997, ApJ, 482, 796 (NL97)
- Oey M. S., Clarke C. J., 1997, MNRAS, 289, 570
- Oppenheimer B. D., Davé R., Kereš D., Fardal M., Katz N., Kollmeier J. A., Weinberg D. H., 2010, MNRAS, 406, 2325
- Ossenkopf V., Henning T., 1994, A&A, 291, 943
- Ostriker E. C., McKee C. F., Leroy A. K., 2010, ApJ, 721, 975
- Pettitt A. R., Dobbs C. L., Acreman D. M., Price D. J., 2014, MNRAS, 444, 919
- Piontek R. A., Ostriker E. C., 2005, ApJ, 629, 849
- Richings A. J., Schaye J., Oppenheimer B. D., 2014, MNRAS, 440, 3349
- Rogers H., Pittard J. M., 2013, MNRAS, 431, 1337
- Salmon J. K., Warren M. S., 1994, J. Comput. Phys., 111, 136
- Salpeter E. E., 1955, ApJ, 121, 161
- Saury E., Miville-Deschénes M.-A., Hennebelle P., Audit E., Schmidt W., 2014, A&A, 567, A16
- Schneider N. et al., 2011, A&A, 529, A1
- Schruba A. et al., 2011, AJ, 142, 37
- Seifried D., Schmidt W., Niemeyer J. C., 2011, A&A, 526, A14
- Sembach K. R., Howk J. C., Ryans R. S. I., Keenan F. P., 2000, ApJ, 528, 310
- Shetty R., Ostriker E. C., 2012, ApJ, 754, 2
- Shetty R., Kelly B. C., Bigiel F., 2013, MNRAS, 430, 288
- Slyz A. D., Devriendt J. E. G., Bryan G., Silk J., 2005, MNRAS, 356, 737
- Smith R. J., Glover S. C. O., Clark P. C., Klessen R. S., Springel V., 2014, MNRAS, 441, 1628
- Spitzer L., Jr, 1942, ApJ, 95, 329
- Springel V., 2005, MNRAS, 364, 1105
- Stinson G. S., Bailin J., Couchman H., Wadsley J., Shen S., Nickerson S., Brook C., Quinn T., 2010, MNRAS, 408, 812
- Stinson G. S., Brook C., Macciò A. V., Wadsley J., Quinn T. R., Couchman H. M. P., 2013, MNRAS, 428, 129
- Stone J. M., Gardiner T. A., Teuben P., Hawley J. F., Simon J. B., 2008, ApJS, 178, 137
- Sutherland R. S., Dopita M. A., 1993, ApJS, 88, 253
- Tacconi L. J. et al., 2013, ApJ, 768, 74
- Tammann G. A., Loeffler W., Schroeder A., 1994, ApJS, 92, 487
- Teyssier R., 2002, A&A, 385, 337
- Tielens A. G. G. M., 2005, The Physics and Chemistry of the Interstellar Medium. Cambridge Univ. Press, Cambridge
- Toalá J. A., Arthur S. J., 2011, ApJ, 737, 100
- Turk M. J., Smith B. D., Oishi J. S., Skory S., Skillman S. W., Abel T., Norman M. L., 2011, ApJS, 192, 9
- van Dishoeck E. F., Black J. H., 1988, ApJ, 334, 771
- Vazquez-Semadeni E., 2009, preprint ([arXiv:0902.0820](https://arxiv.org/abs/0902.0820))
- Waagan K., 2009, J. Comput. Phys., 228, 8609
- Waagan K., Federrath C., Klingenberg C., 2011, J. Comput. Phys., 230, 3331
- Walch S., Naab T., 2015, MNRAS, 451, 2757
- Walch S., Wünsch R., Burkert A., Glover S., Whitworth A., 2011, ApJ, 733, 47
- Walch S. K., Whitworth A. P., Bisbas T., Wünsch R., Hubber D., 2012, MNRAS, 427, 625
- Walch S., Whitworth A. P., Bisbas T. G., Wünsch R., Hubber D. A., 2013, MNRAS, 435, 917
- Wetzstein M., Nelson A. F., Naab T., Burkert A., 2009, ApJS, 184, 298
- Wolfire M. G., Hollenbach D., McKee C. F., Tielens A. G. G. M., Bakes E. L. O., 1995, ApJ, 443, 152
- Wolfire M. G., McKee C. F., Hollenbach D., Tielens A. G. G. M., 2003, ApJ, 587, 278
- Übler H., Naab T., Oser L., Aumer M., Sales L. V., White S. D. M., 2014, MNRAS, 443, 2092

This paper has been typeset from a TeX/LaTeX file prepared by the author.